Rotor Vibration Reduction Using Multi-Element Multi-Path Design

by

Keye Su

Department of Mechanical Engineering and Materials Science
Duke University

Date:_____

Approved:

_____
Donald B. Bliss, Supervisor

_____
Laurens E. Howle

_____
Linda P. Franzoni

Thesis submitted in partial fulfillment of
the requirements for the degree of
Master of Science in the Department of
Mechanical Engineering and Materials Science in the Graduate School
of Duke University

2013

ABSTRACT

Rotor Vibration Reduction Using Multi-Element Multi-Path Design

by

Keye Su

Department of Mechanical Engineering and Materials Science
Duke University

Date:_____
Approved:

_____
Donald B. Bliss, Supervisor

_____
Laurens E. Howle

_____
Linda P. Franzoni

An abstract of a thesis submitted in partial
fulfillment of the requirements for the degree
of Master of Science in the Department of
Mechanical Engineering and Materials Science in the Graduate School of
Duke University

2013

Abstract

Multi-Element Multi-Path (MEMP) structural design is a new concept for rotor vibration reduction. This thesis explores the possibility of applying MEMP design to helicopter rotor blades. A conceptual design is developed to investigate the MEMP blade's vibration reduction performance. In the design, the rotor blade is characterized by two centrifugally loaded beams which are connected to each other through linear and torsional springs. A computer program is built to simulate the behavior of such structures. Detailed parametric studies are conducted. The main challenges in this thesis involve the blade hub load vibration analysis, the blade thickness constraint and the blade parameter selection. The results show substantial vibration reduction for the MEMP design but the large relative deflection between the two beams, conceptualized as an internal spar and airfoil shell, remains a problem for further study.

Contents

List of Figures

List of Tables

List of Symbols

T	Tension in the beam
ρ	Mass per unit length
Ω	Blade rotation rate
L	Length of the beam
E	Young's modulus
I	Area moment of inertia
ω	Harmonic excitation frequency
p	Amplitude of harmonic excitation
S	Spring stiffness
m_1, m_2	Moment in the beam
μ	Torsional spring stiffness of the first kind (in phase)
υ	Torsional spring stiffness of the second kind (out of phase)
k_h	Boundary linear spring stiffness
k_a	Boundary torsional spring stiffness
$\tilde{y}$	Nondimensional deflection
$\tilde{x}$	Nondimensional radial position
$\tilde{t}$	Nondimensional time
λ	Nondimensional bending stiffness

S_c	Nondimensional spring stiffness
P	Nondimensional distributed force amplitude
K_h	Nondimensional boundary spring stiffness
K_a	Nondimensional boundary torsional spring stiffness
$\tilde{\mu}$	Nondimensional torsional spring stiffness of the first kind
$\tilde{\upsilon}$	Nondimensional torsional spring stiffness of the second kind
F_{point}	End point force
$\tilde{h}$	Nondimensional deflection amplitude
a_n	Cosine component of aerodynamic force
b_n	Sine component of aerodynamic force
f_{aero}	Aerodynamic force
Δy	Relative deflection
$\tilde{F}_{hub}$	Hub load

Acknowledgements

I should first thank my advisor, Dr. Donald Bliss for his constant guidance and help. Over the past two years, he is more than an advisor. His unique insight and creative analysis to academic problems has earned me invaluable research skills. His useful advice and prompt help have got me through many difficulties. In addition, I wish to thank Dr. Laurens Howle and Dr. Linda Franzoni for being on my committee. My thanks are also given to Dr. Earl Dowell for constantly encouraging my work.

The next people I wish to thank are my parents who are the most important in my life. Without their support, I am not able to study at Duke. Their persistent love has help me reach this far and will motivate me to achieve more.

Finally, my thanks are due to all the people in the department of Mechanical Engineering and Material Science for giving me this opportunity to study in such a friendly environment. I am also thankful to my fellow graduate student Jiadong and Chen. I am really happy being with them during this wonderful two years.

1. Introduction

1.1 Problem Statement

Rotor blade vibration reduction has become an important consideration in aerospace engineering, turbomachinery, automobile engineering, etc. In the design of rotorcraft and wind turbines there is always a need to reduce the rotor blade vibration to maintain the stability and operational life of the whole structure. The reduction of hub vibration in a helicopter is an important example.

Due to the unique capacity for low speed flight and vertical takeoff, helicopters undertake a variety of military and civil missions that are beyond the capabilities of fixed wing aircraft. However, high vibration and noise levels limit the helicopter's effectiveness. While many sources, including the main rotor, tail rotor, engine, and gearbox, contribute to the overall vibration levels and noise generation, the dominant source of vibration and noise is the main rotor. Vibratory airload transferred from the main rotor to the fuselage have been a critical concern in the rotorcraft development. In addition to passenger comfort, reliability and fatigue life of components are adversely affected by vibration. Thus, an effective method to reduce the rotor blade vibration is needed (Bryan Glaz, 2008).

1.2 Current Applicable Methods

Traditional noise and vibration reduction strategies divide into two general categories: active control and passive control. More recently hybrid approaches have been explored (Lee 2002, Zielinski 2011).

Active method is extensively investigated because of its advantage in high efficiency and easy availability. Active control requires sensors, actuators, accompanying electronic equipment and software, which lead to issues of cost, weight, complexity, and reliability. Active control tends to work best when targeting a single frequency or set of frequencies and not as well for broadband vibrations or noise; and it is typically restricted to low frequency applications (Fuller 1996, Cavallo 2010).

Passive method is the earliest and most widely implemented approach to vibration reduction. Passive reduction strategies involve either the addition of damping or the alteration of the system dynamics. Examples include constrained layer damping, external coatings of damping material, as well as the addition of discrete dampers, all of which add weight to the system. Dynamic passive control may include the addition of discrete oscillators or resonators, individually or as a group (Thompson 2008, Carcaterra 2012). In the latter case, the oscillators can be used in the context of fuzzy structure theory (Ohayon, 1998) or to take advantage of a phenomena known as Anderson localization (Photiadis, 1999). There are also strategies employed specifically for periodic

structures that involve the utilization of stop and pass band behavior (Bansal 1997, Legault 2009, Silva 1991). Passive control may be able to target a broader frequency range than active control and functions best at higher frequencies. The drawbacks of using passive control are the added weight and space requirements.

In many ways, a passive method is superior to an active method. Rather than placing active components in the structure, the passive structural design is instead modified to produce the desired characteristics. An example is structural optimization, where a computer simulation attempts to calculate a design meeting certain criteria iteratively. The passive approach is more fail-safe because there are no discrete actuators or power sources which can fail. With passive devices such as absorbers, the possibility of failure is present, but for elastic tailoring, the vibration treatment fails only when the major structural component itself fails (Matthew W. Floros, 2000).

1.3 Study of MEMP structure as the solution

Due to the limitations for both passive and active methods, a novel method to solve the vibration problem is highly demanded. Based on prior work, the MEMP structure promises an effective way to deal with vibration problem while maintaining several advantages which otherwise lose if using current methods. The result from noise reduction performance of MEMP structure has demonstrated its effective and efficient

capacity to diminish high frequency vibration. While the rotor blade holds certain unique property from normal structures, such as centrifugal force, limited space and fluid-solid interaction, most part of physical model is similar to others, which shows promising future for application of MEMP structure.

1.4. The MEMP Concept

The approach to be explored in this thesis to solve vibration problem is the multi-element multi-path (MEMP) structures that inherently suppress vibration. Figure 1 shows examples represented as beams. If the beam is driven harmonically at one end and fixed at the other end, like the beams in Figure 1, the drive point can be viewed as the source of waves traveling in one direction. Waves propagating in the opposite direction are produced by reflection from the fixed end; these waves in turn reflect from the drive point end, etc. If a structure does not support wave propagation, extended vibration will not occur beyond a drive point region.

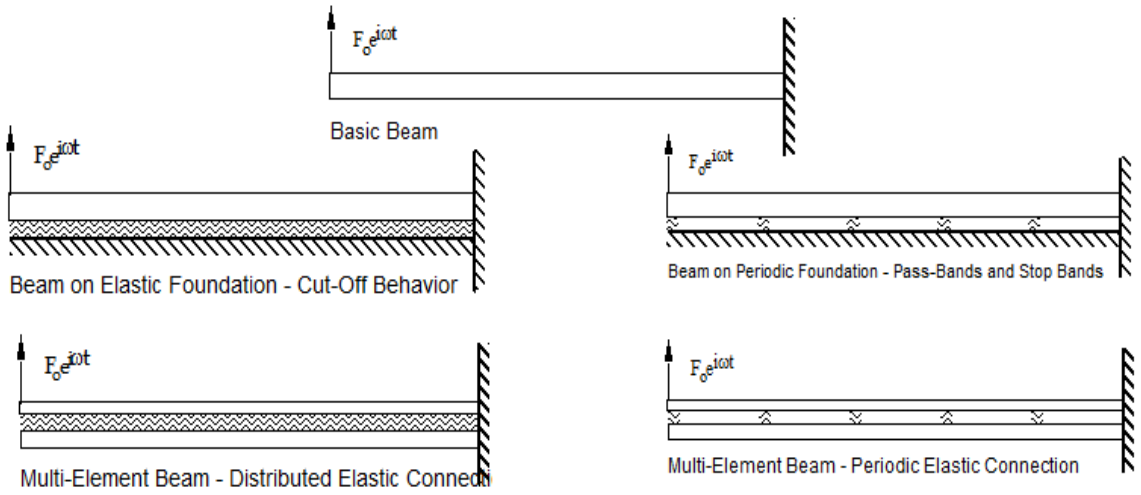

Figure 1: Basic Beams, some with suspensions attached to ground, versus MEMP (Multi-Element/Multi-Path) Beams with distributed and periodic interconnections.

There are several ways to suppress wave propagation on a beam. One of them is described below. If a beam is placed on a distributed elastic suspension attached to ground, see Figure 1, then below a critical frequency a "cut-off" phenomenon occurs whereby waves do not propagate and disturbances decay spatially, i.e. they are evanescent. The motion of the beam is localized in the region around the drive point, although no damping has been introduced. In this case, vibration reduction has been achieved through a mismatch of the dynamic processes at work on the beam.

Another approach is to attach structural discontinuities to the beam at regular intervals, also shown in Figure 1. As is well known, this periodic structure will exhibit an alternating series of pass-bands for wave propagation and stop-bands for no wave

propagation versus frequency. Whenever the harmonic forcing frequency lies in a stop band, the vibratory motion will be confined to the spatial region around the drive point due to the evanescent nature of the wave solutions. The forces at the fixed end will be small, and there will be no resonant behavior in stop bands. Again this effect is achieved with purely reactive connections (no damping). The dispersion relation governing the dependence of wavenumber on frequency is modified by the addition of new physical effects (a suspension or periodic discontinuities) to the equations (Donald B. Bliss, 2008).

Simulations using model problems suggest the development of structures that exhibit evanescent wave behavior to reduce vibration is very promising. This approach has not been extensively investigated, perhaps because of a perceived shortcoming in the above examples. Once the suspension or periodic discontinuities are added, the structure may no longer be self-contained. For instance, adding the suspension to the beam requires that the other side of the suspension be attached to ground, which means the structure must rely on external contact to achieve the desired effect. This external contact is not a possibility for many practical structures, but fortunately it is actually not needed. The behavior of such MEMP structures will be studied later in this thesis, the purpose of which is to investigate the possibility of applying this design to helicopter rotor blade. A conceptual design using realistic parameters is developed for the purpose of assessing whether the idea is feasible.

2. Physical Modeling

2.1 Introduction

This chapter describes the physical models considered during the course of this work. They fall into the following two categories.

1. Single beam model

2. MEMP beam model

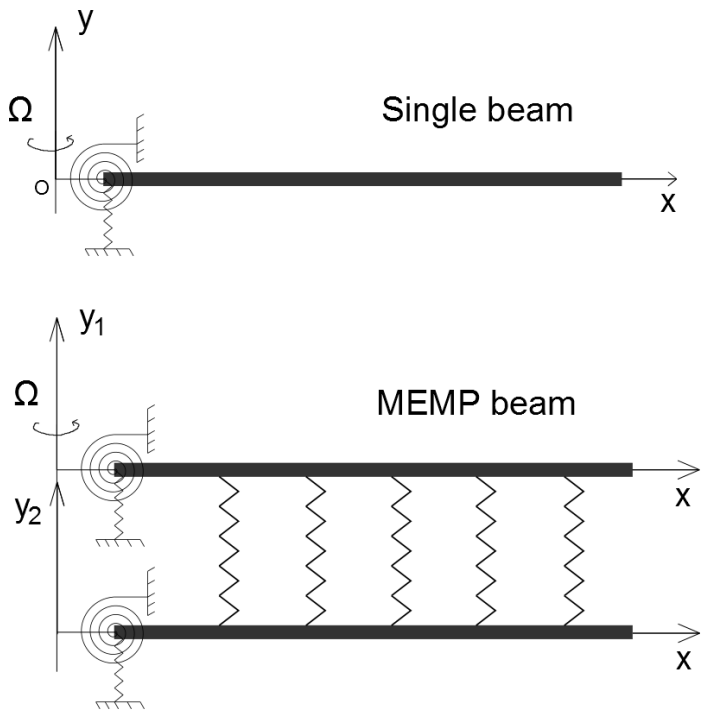

Figure 2: Single beam model and MEMP beam model

These two physical models are mechanical simplification of traditional rotor blades and MEMP blades. The goal for developing such two models is to obtain maximum physical insight while keeping the mathematics simple. Both models and

their modifications are designed to allow specific parametric studies and comparisons. The following sections will give the details of these two types of models and their modifications.

2.2 Traditional Rotor Blade Design

Figure 3 shows the traditional rotor structure to be modeled.

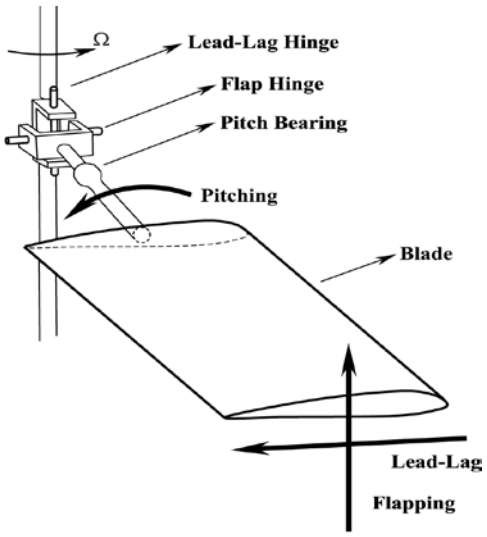

Figure 3: Traditional rotor blade design. Image from www.emeraldinsight.com

The traditional rotor consists of a long thin blade and a mechanical attachment linkage between the blade and the hub. The mechanical linkage primarily consists of a lead-lag hinge and a flapping hinge, which allow the blade to have lead-lag motion in horizontal plane and flap in vertical plane. The rotation of the rotor is driven by the

rotor shaft. In operation, the blade undergoes bending and torsional vibration. The latter one is not considered in this thesis.

2.2.1 Single Beam Model

The single beam model is used to model the traditional rotor blade design. It is displayed in Figure 4. In this model, only bending vibration will be considered and will be assumed that linear theory applies. The traditional blade is characterized as a centrifugal loaded beam connected to a rotor shaft through a linear and a torsional spring. By measuring the displacement of the linear spring, the hub force can be calculated. In the same manner, the hub moment can be obtained by measuring the torsional spring's displacement. As the lead-lag motion in horizontal plane is beyond of the subject of this thesis, the motion in that direction is not considered.

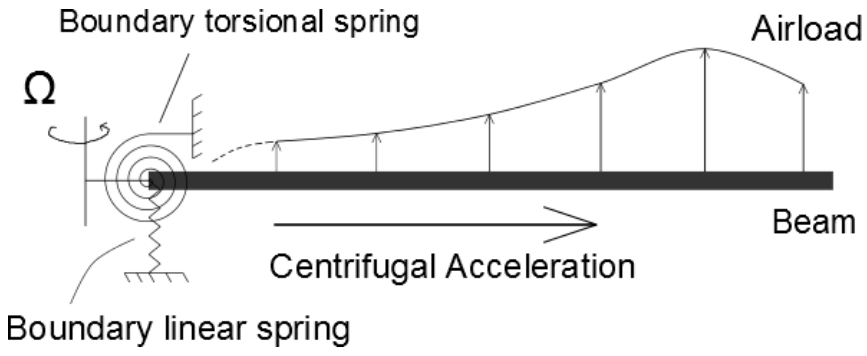

Figure 4: Single beam model

2.2.2 Modified Single Beam Model

The modified single beam model is the same as single beam model except that the beam is hooked to the ground through springs. Figure 5 shows the difference. This model is used to initially explore the MEMP concept.

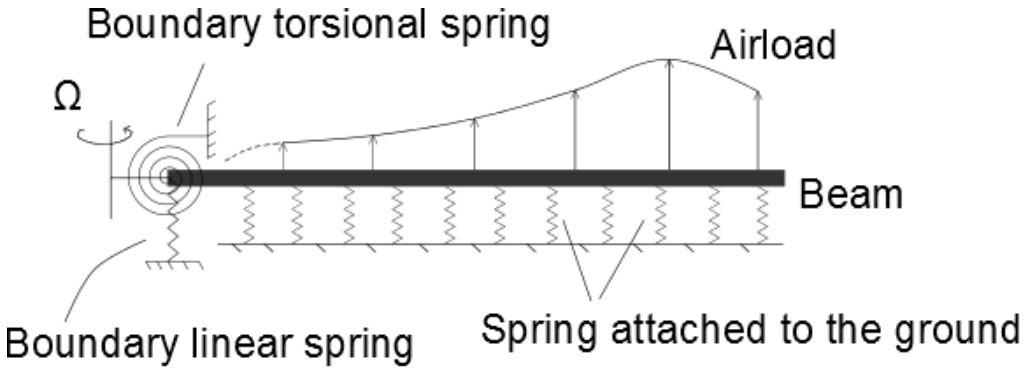

Figure 5: Modified single beam model

2.3 MEMP Rotor Blade Design

Figure 6 illustrates the MEMP rotor design, which differs from the traditional design in blade structure.

In MEMP design, the rotor blade has two components: the spar and the shell. They are clearly indicated in the Figure 6. The spar is the inner structure of rotor blade which connects with the shell using springs and dampers. The shell encases the spar completely and withstands the aerodynamic force. This layered structure plays a critical

role on reducing the hub vibration, which will be well studied in the next several chapters. At the root of blade, both spar and shell are linked to the rotor shaft through separate mechanical attachment.

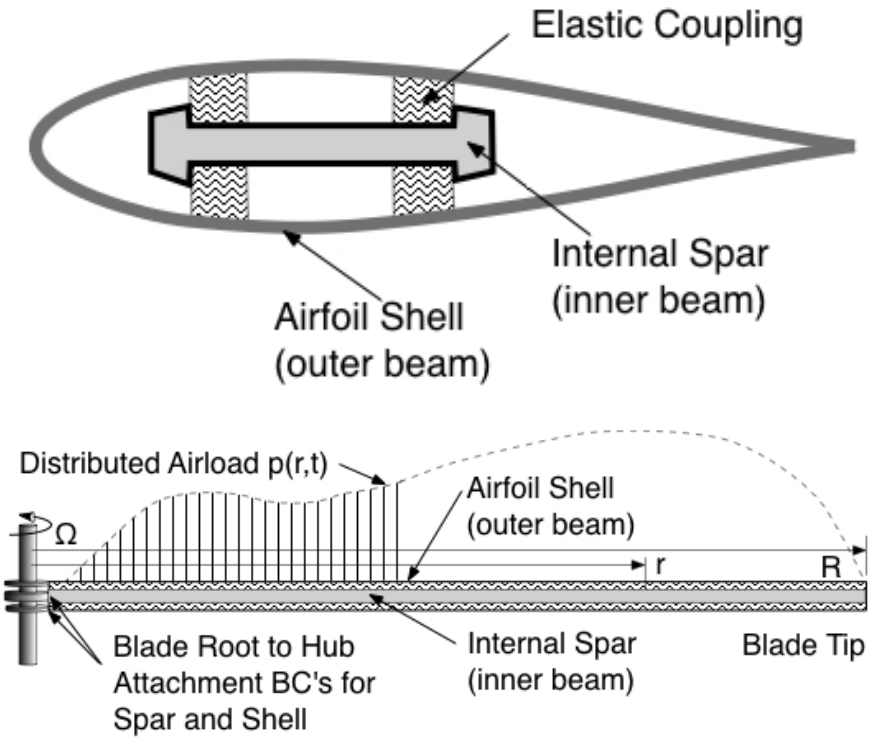

Figure 6: MEMP blade design

2.3.1 MEMP Beam Model

The MEMP beam model, shown in Figure 7, is a sufficient physical description of MEMP rotor blade design. In this model, the blade spar and shell are characterized as two beams connected with springs and dampers. To maintain the whole system's static strength, there are also torsional springs between the two beams. They prevent beams from bending too much under static load. At the root, the two mechanical attachments are simplified as torsional and linear springs.

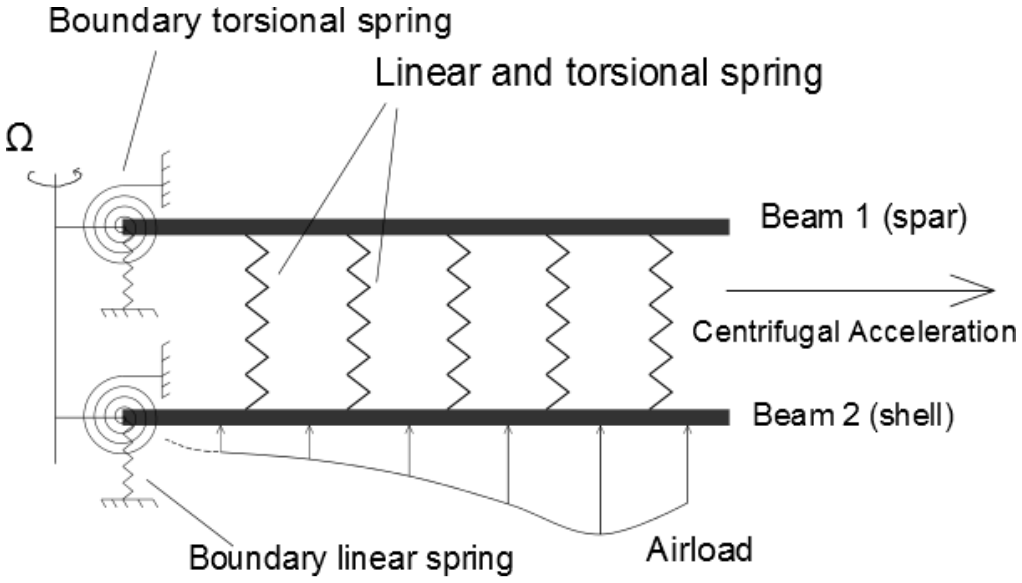

Figure 7: MEMP blade model

2.3.2 Some Example Modifications

The first important modification is displayed in Figure 8. In this model, there is no blade attachment for the shell at the root. It is totally free at root as well as at tip.

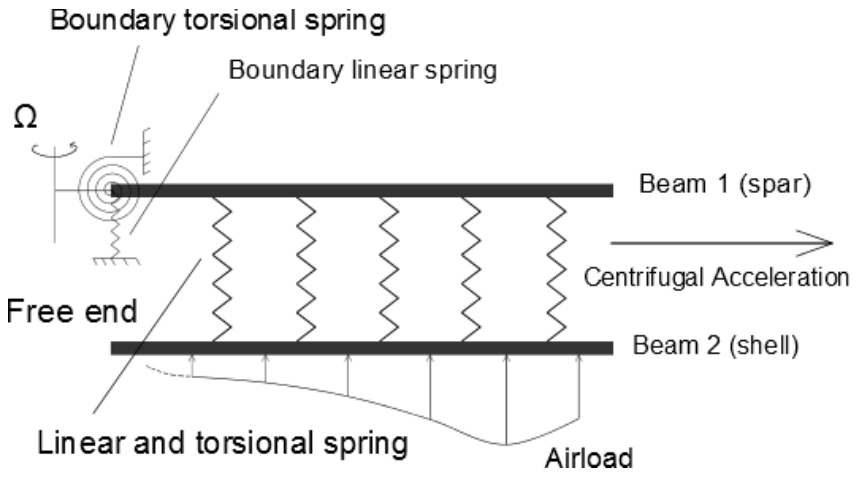

Figure 8: First modification

The second modification is shown in Figure 9. It replaces the springs (both linear and torsional springs) between the two beams with rigid connection. This is a modification of great use because it is an effective way to transforms the MEMP beam model to single beam model.

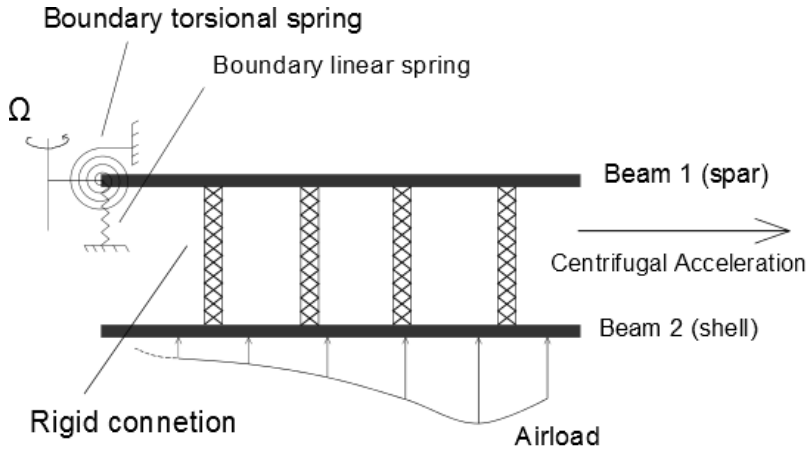

Figure 9: Second Modification

2.4 Aerodynamic Force

When in operation, the rotating blades generate aerodynamic force. This aerodynamic force depends not only on radial position but also on time as the rotatory blade changes azimuthal position. In the two models considered above, the aerodynamic forces fall into two categories: the point aerodynamic force and the distributed aerodynamic force, as shown in Figure 10 and Figure 11. Both types of aerodynamic forces are harmonic forces but with different amplitude. For the point aerodynamic force, it only applied at the tip of the beams. Though point force has little practical meaning, it provides a fast way to test the physical models since it is mathematically and numerically simple. For the distributed aerodynamic force, it applies along the whole beam with different value. This kind of aerodynamic force models the case that happens in reality. There are many kinds of distributions according to different rotor types and different operating conditions.

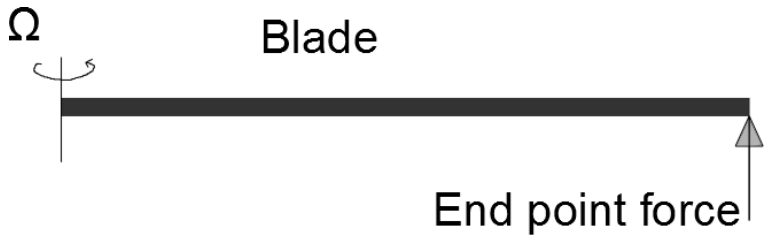

Figure 10: Point force at the tip

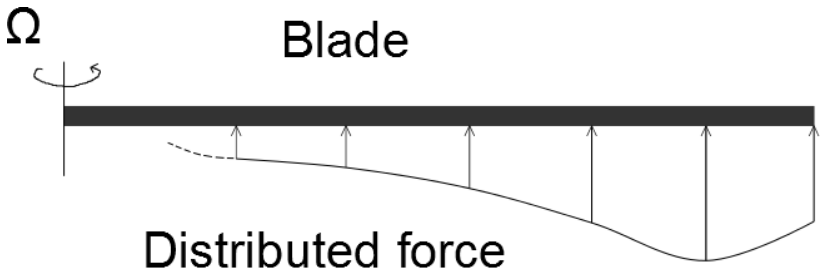

Figure 11: Force distribution along radial location

3. Mathematical Modeling

3.1 Introduction

This chapter develops the mathematical equations and the associated computer solver for the physical models. As discussed in previous chapter, the physical models are of the following types:

1. Single beam model.

2. MEMP beam model.

The mathematical description of single beam model and modified single beam model requires the solution of a differential equation having the general forms below:

$$\frac{\partial^2 y}{\partial t^2} = A\frac{\partial^4 y}{\partial x^4} + B\frac{\partial}{\partial x}[(1-x^2)\frac{\partial y}{\partial x}] + Cy \tag{4.1}$$

The mathematical description of MEMP beam model and its modification require the solution of the coupled differential equations having the general forms below:

$$\frac{\partial^2 y_1}{\partial t^2} = A\frac{\partial^4 y_1}{\partial x^4} + B\frac{\partial}{\partial x}[(1-x^2)\frac{\partial y_1}{\partial x}] + C(\frac{\partial y_1}{\partial x} - \frac{\partial y_2}{\partial x}) + D(\frac{\partial y_1}{\partial x} + \frac{\partial y_2}{\partial x}) + E(y_1 - y_2) \tag{4.2}$$

$$\frac{\partial^2 y_2}{\partial t^2} = A\frac{\partial^4 y_2}{\partial x^4} + B\frac{\partial}{\partial x}[(1-x^2)\frac{\partial y_2}{\partial x}] + C(\frac{\partial y_2}{\partial x} - \frac{\partial y_1}{\partial x}) + D(\frac{\partial y_2}{\partial x} + \frac{\partial y_1}{\partial x}) + E(y_2 - y_1) \tag{4.3}$$

It is very difficult to find closed-form analytical solutions for these variable coefficient differential equations except in some special cases. For engineering problems, however, it is sufficient if they are solved by numerical methods. In this thesis, Wolfram

Mathematica is used to compute the numerical solution. The next sections of this chapter will discuss the physical meaning of these differential equations, the nondimentional parameters, and the computer algorithm.

3.2 Centrifugal Effect

One aspect that differentiates rotor blades from other problems is the centrifugal effect. The strong centrifugal acceleration due to rotation results in non-uniform tension along the blade which complicates the problem, thus the variable coefficient mathematical equations. Figure 11 describes the coordinate system of single beam model. The x axis represents the radius of blade while the y axis represents the beam deflection. To obtain the tension due to centrifugal acceleration, a small section of beam is considered.

Assuming at x and x + dx, the tension in the beam is T and T+dT, then

$$T-(T+dT)=-\rho(dx)\Omega^2 x$$

where

ρ - Mass per unit length

Ω - Blade rotation rate

Therefore $dT=--\rho\Omega^2 xdx$

Assuming the length of blade equals to L and the tension drops down to zero at the tip of the blade, integrating the equation from x to L gives,

$$T = \frac{1}{2}\rho\Omega^2(L^2 - x^2) \tag{4.4}$$

This is the function of tension with respect to position. It will appear later in this chapter without further explanation.

3.3 Mathematical Modeling for Single Beam Model

Figure 12 describes the coordinate system of single beam model. There are four factors in the single beam model that affect the motion of the beam: the inertia, the bending stiffness, the distributed aerodynamic force and the tension due to rotation. They are discussed in detail below.

Figure 12: Coordinate system of single beam model

For a unit length of the beam, the inertia term can be written as

$$\rho \frac{\partial^2 y}{\partial t^2}$$

Assuming the Young's modulus and the moment of inertia to be E and I, the bending stiffness term has the form below,

$$-EI \frac{\partial^4 y}{\partial x^4}$$

The distributed aerodynamic force can be written as $p(x)e^{i\omega t}$. For simplicity, it is denoted as $pe^{i\omega t}$, where ω is the harmonic excitation frequency.

The tension term can be expressed as

$$\frac{\partial}{\partial x}(T \frac{\partial y}{\partial x})$$

From the previous section, the tension along the beam equals to $\frac{1}{2}\rho\Omega^2(L^2 - x^2)$

Therefore, $\frac{\partial}{\partial x}(T \frac{\partial y}{\partial x}) = \frac{1}{2}\rho\Omega^2 \frac{\partial}{\partial x}[(L^2 - x^2)\frac{\partial y}{\partial x}]$

Finally, the mathematical description for single beam model is as follow.

$$\rho \frac{\partial^2 y}{\partial t^2} = -EI \frac{\partial^4 y}{\partial x^4} + \frac{1}{2}\rho\Omega^2 \frac{\partial}{\partial x}[(L^2 - x^2)\frac{\partial y}{\partial x}] + pe^{i\omega t} \quad (4.5)$$

In the modified single beam model, the beam is hooked with ground by springs. This will add another term in the equation. Assume the spring stiffness for a unit length of beam to be S. Then the modified equation is shown below.

$$\rho \frac{\partial^2 y}{\partial t^2} = -EI \frac{\partial^4 y}{\partial x^4} + \frac{1}{2} \rho \Omega^2 \frac{\partial}{\partial x}[(L^2 - x^2) \frac{\partial y}{\partial x}] + pe^{i\omega t} + Sy \tag{4.6}$$

As stated in the previous section, it is difficult to find purely analytical solutions for equation (4.5) and (4.6).

3.4 Mathematical Modeling for MEMP Beam Model

Figure 13 describes the coordinate system of MEMP beam model.

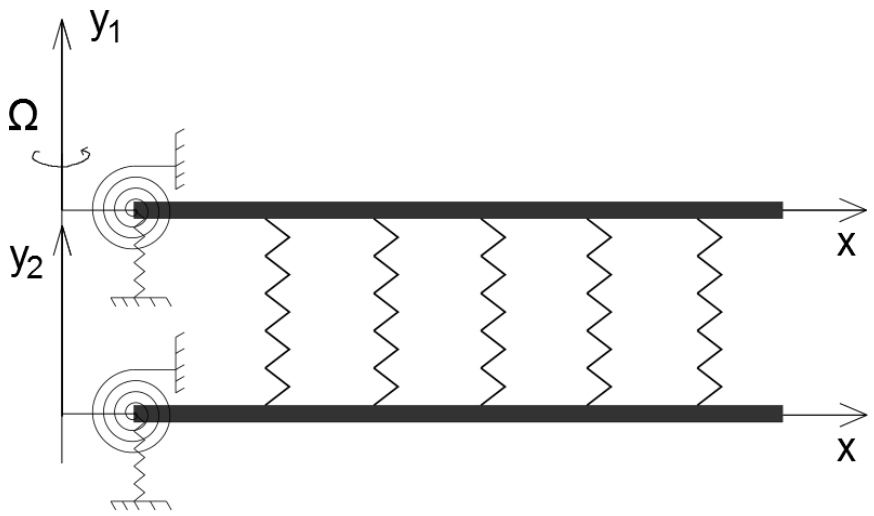

Figure 13: Coordinate system of MEMP beam model

There are six factors in the MEMP beam model that affect the motion of the beam:

1. Inertia

2. Bending stiffness

3. Tension due to rotation

4. Torsional spring of the first kind

5. Torsional spring of the second kind

6. Linear spring

7. Distributed aerodynamic force: this only applies to the shell (the second beam).

In last section, the first three factors are discussed. Figure 14 shows the mechanism of the two kinds of torsional springs. The first bends both beams the same way while the second bends them the opposite way. To mark the effect of these two kinds of torsional springs, another two terms need to be added in mathematical description.

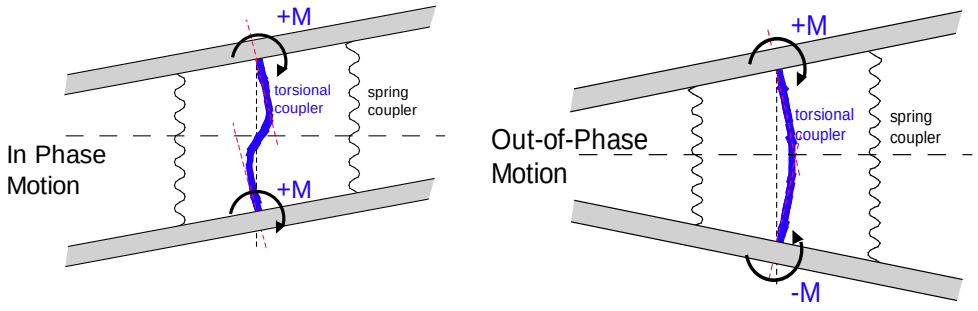

Figure 14: Torsional Spring

The torsional spring stiffness is defined in terms of the moment provided by a unit length of beam with a unit degree of angular deflection. That is, for the first beam (the spar in MEMP design)

$$m_1 = \mu(\frac{\partial y_1}{\partial x} - \frac{\partial y_2}{\partial x}) + \upsilon(\frac{\partial y_1}{\partial x} + \frac{\partial y_2}{\partial x})$$

For the second beam (the shell in MEMP design)

$$m_2 = \mu(\frac{\partial y_2}{\partial x} - \frac{\partial y_1}{\partial x}) + \upsilon(\frac{\partial y_1}{\partial x} + \frac{\partial y_2}{\partial x})$$

where

m_1 - Moment per unit length applied in the first beam

m_2 - Moment per unit length applied in the second beam

μ - Torsional spring stiffness of the first kind (in phase)

υ - Torsional spring stiffness of the second kind (out of phase)

The associated shear force can be derived by analyzing the moment balance on a small section of the beam. In Figure 15, the moment contribution from torsional spring needs to balance with the moment generated by the associated shear force.

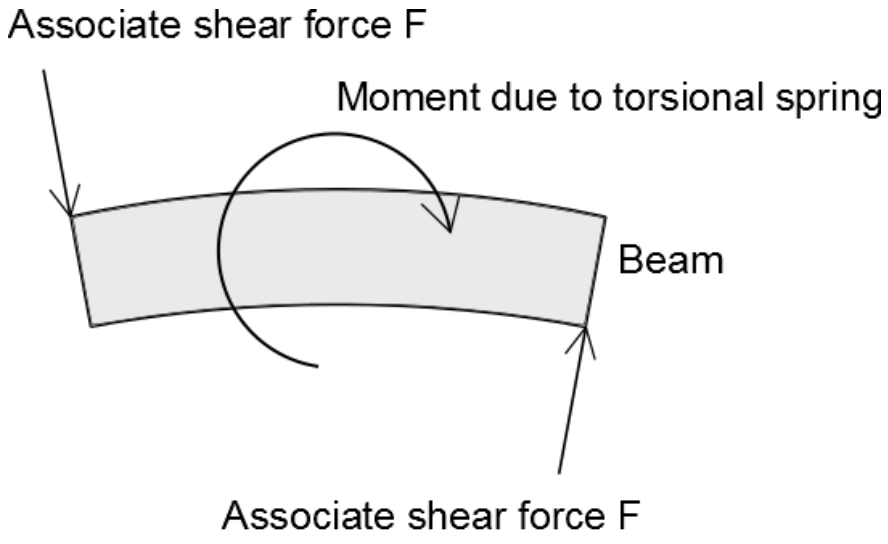

Figure 15: Shear force associated with torsional spring

That is,

$$F_1 \cdot dx = \mu \cdot dx(\frac{\partial^2 y_1}{\partial x^2} - \frac{\partial^2 y_2}{\partial x^2}) + \upsilon \cdot dx(\frac{\partial^2 y_1}{\partial x^2} + \frac{\partial^2 y_2}{\partial x^2})$$
$$F_2 \cdot dx = \mu \cdot dx(\frac{\partial^2 y_2}{\partial x^2} - \frac{\partial^2 y_1}{\partial x^2}) + \upsilon \cdot dx(\frac{\partial^2 y_1}{\partial x^2} + \frac{\partial^2 y_2}{\partial x^2})$$

Therefore

$$\begin{aligned} F_1 &= \mu(\frac{\partial^2 y_1}{\partial x^2} - \frac{\partial^2 y_2}{\partial x^2}) + \upsilon(\frac{\partial^2 y_1}{\partial x^2} + \frac{\partial^2 y_2}{\partial x^2}) \\ F_2 &= \mu(\frac{\partial^2 y_2}{\partial x^2} - \frac{\partial^2 y_1}{\partial x^2}) + \upsilon(\frac{\partial^2 y_1}{\partial x^2} + \frac{\partial^2 y_2}{\partial x^2}) \end{aligned} \tag{4.7}$$

This is the shear force contribution from torsional spring.

The linear spring mathematical description for MEMP beam model is the same as that in the modified single beam model except for the coupled displacement. The force per unit length due to linear spring equals to $S(y_1 - y_2)$ for the first beam and $S(y_2 - y_1)$ for the second beam.

The distributed aerodynamic force can be written as $p(x)e^{i\omega t}$. For simplicity, it is denoted as $pe^{i\omega t}$. It only applies on the shell (the second beam in MEMP beam model).

Finally, the mathematical description of MEMP beam model is as follow,

$$\rho\frac{\partial^2 y_1}{\partial t^2}=-EI\frac{\partial^4 y_1}{\partial x^4}+\frac{1}{2}\rho\Omega^2\frac{\partial}{\partial x}[(1-x^2)\frac{\partial y_1}{\partial x}]+\mu(\frac{\partial^2 y_1}{\partial x^2}-\frac{\partial^2 y_2}{\partial x^2})$$
$$+\upsilon(\frac{\partial^2 y_1}{\partial x^2}+\frac{\partial^2 y_2}{\partial x^2})+S(y_1-y_2)$$
$$\rho\frac{\partial^2 y_2}{\partial t^2}=-EI\frac{\partial^4 y_2}{\partial x^4}+\frac{1}{2}\rho\Omega^2\frac{\partial}{\partial x}[(1-x^2)\frac{\partial y_2}{\partial x}]+\mu(\frac{\partial^2 y_2}{\partial x^2}-\frac{\partial^2 y_1}{\partial x^2}) \quad (4.8)$$
$$+\upsilon(\frac{\partial^2 y_1}{\partial x^2}+\frac{\partial^2 y_2}{\partial x^2})+S(y_2-y_1)+pe^{i\omega t}$$

If the properties of two beams are different, equation (4.7) evolves to

$$\rho_1\frac{\partial^2 y_1}{\partial t^2}=-E_1I_1\frac{\partial^4 y_1}{\partial x^4}+\frac{1}{2}\rho_1\Omega^2\frac{\partial}{\partial x}[(1-x^2)\frac{\partial y_1}{\partial x}]+\mu(\frac{\partial^2 y_1}{\partial x^2}-\frac{\partial^2 y_2}{\partial x^2})$$
$$+\upsilon(\frac{\partial^2 y_1}{\partial x^2}+\frac{\partial^2 y_2}{\partial x^2})+S(y_1-y_2)$$
$$\rho_2\frac{\partial^2 y_2}{\partial t^2}=-E_2I_2\frac{\partial^4 y_2}{\partial x^4}+\frac{1}{2}\rho_2\Omega^2\frac{\partial}{\partial x}[(1-x^2)\frac{\partial y_2}{\partial x}]+\mu(\frac{\partial^2 y_2}{\partial x^2}-\frac{\partial^2 y_1}{\partial x^2}) \quad (4.9)$$
$$+\upsilon(\frac{\partial^2 y_1}{\partial x^2}+\frac{\partial^2 y_2}{\partial x^2})+S(y_2-y_1)+pe^{i\omega t}$$

Equation (4.5), (4.6), (4.7) and (4.8) are differential equations of 4th order. Thus they need four boundary conditions for each equation to construct a full mathematical description.

3.5 Boundary Condition

There are four possible quantities that can be specified as boundary conditions for these two physical models. They are listed below,

1. Beam deflection

2. Beam slope, which is the first derivative of beam deflection

3. Moment across the beam, which is proportional to the second derivative of beam deflection

4. Shear force across the beam, which is proportional to the third derivative of beam deflection

In both models, the beams' roots and tips are either free or connected with springs. Deflection and slope are unknowns. Only moment and shear force can be calculated.

3.5.1 Single Beam Model

In the single beam model, the total vertical force and moment should be zero at the root. Thus,

$$-EI\frac{\partial^3 y}{\partial x^3}+\frac{1}{2}\rho\Omega^2 L^2\frac{\partial y}{\partial x}-k_h y=0 \tag{4.10}$$

where k_h - Boundary linear spring stiffness

$$EI\frac{\partial^2 y}{\partial x^2}-k_a\frac{\partial y}{\partial x}=0 \tag{4.11}$$

where k_a - Boundary torsional spring stiffness

At the tip, since there is no external moment, the bending moment equals to zero.

$$EI\frac{\partial^2 y}{\partial x^2}=0 \tag{4.12}$$

The shear force equals to the end point force if any.

$$-EI\frac{\partial^3 y}{\partial x^3}=F_{point} \tag{4.13}$$

3.5.2 MEMP Beam Model

In MEMP beam model, however, the boundary condition is more complicated. At the root, the vertical force has four contributions: shear force due to bending, shear force due to torsional springs (discussed in previous section), vertical component of tension and the boundary spring force. Thus,

For the first beam,

$$-E_1I_1\frac{\partial^3 y_1}{\partial x^3}+\frac{1}{2}\rho_1\Omega^2L^2\frac{\partial y_1}{\partial x}+\mu(\frac{\partial^2 y_1}{\partial x^2}-\frac{\partial^2 y_2}{\partial x^2})+\upsilon(\frac{\partial^2 y_1}{\partial x^2}+\frac{\partial^2 y_2}{\partial x^2})-k_{h1}y_1=0 \tag{4.14a}$$

For the second beam,

$$-E_2I_2\frac{\partial^3 y_2}{\partial x^3}+\frac{1}{2}\rho_2\Omega^2L^2\frac{\partial y_2}{\partial x}+\mu(\frac{\partial^2 y_2}{\partial x^2}-\frac{\partial^2 y_1}{\partial x^2})+\upsilon(\frac{\partial^2 y_1}{\partial x^2}+\frac{\partial^2 y_2}{\partial x^2})-k_{h2}y_2=0 \tag{4.14b}$$

The total moment should also be zero at the root for both beams.

$$k_{a1}\frac{\partial y_1}{\partial x}-E_1I_1\frac{\partial^2 y_1}{\partial x^2}=0 \tag{4.15a}$$

$$k_{a2}\frac{\partial y_2}{\partial x} - E_2 I_2 \frac{\partial^2 y_2}{\partial x^2} = 0 \tag{4.15b}$$

At the tip, since there is no external moment for both beams,

$$-E_1 I_1 \frac{\partial^2 y_1}{\partial x^2} = 0 \tag{4.16a}$$

$$-E_2 I_2 \frac{\partial^2 y_2}{\partial x^2} = 0 \tag{4.16b}$$

The total shear force should be equal to 0 for the first beam and the end point force for the second beam as only the second beam (shell) withstands aerodynamic force,

$$-E_1 I_1 \frac{\partial^3 y_1}{\partial x^3} + \mu\left(\frac{\partial^2 y_1}{\partial x^2} - \frac{\partial^2 y_2}{\partial x^2}\right) + \upsilon\left(\frac{\partial^2 y_1}{\partial x^2} + \frac{\partial^2 y_2}{\partial x^2}\right) = 0 \tag{4.17a}$$

$$-E_2 I_2 \frac{\partial^3 y_2}{\partial x^3} + \mu\left(\frac{\partial^2 y_2}{\partial x^2} - \frac{\partial^2 y_1}{\partial x^2}\right) + \upsilon\left(\frac{\partial^2 y_1}{\partial x^2} + \frac{\partial^2 y_2}{\partial x^2}\right) = F_{point} \tag{4.17b}$$

Equation (4.10) ~ (4.17) describe the boundary conditions for the single beam model and the MEMP beam model. Finally, the combination of equation (4.5), (4.10), (4.11), (4.12) and (4.13) constitutes a full mathematical description of the single beam model. The combination of equation (4.9), (4.14), (4.15), (4.16) and (4.17) constitutes a full mathematical description of the MEMP beam model.

3.6 Nondimensional Equation and Boundary Condition

A nondimensional equation is simpler to solve and analyze. This section discusses the dimensionless mathematical equations and the associated dimensionless boundary conditions.

3.6.1 Single Beam Model

The mathematical conversion is listed below:

$$\tilde{y} = \frac{y}{L}, \tilde{x} = \frac{x}{L}, \tilde{t} = t\Omega$$

$$\lambda = \frac{EI}{\rho\Omega^2 L^4}, S_c = \frac{S}{\rho\Omega^2}, P = \frac{p}{\rho\Omega^2 L}, K_h = \frac{k_h}{\rho\Omega^2 L^2}, K_a = \frac{k_a}{\rho\Omega^2 L^3}$$

Applying the conversion to equation (4.5), it becomes,

$$\frac{\partial^2 \tilde{y}}{\partial \tilde{t}^2} = -\lambda \frac{\partial^4 \tilde{y}}{\partial \tilde{x}^4} + \frac{1}{2}\frac{\partial}{\partial \tilde{x}}[(1-\tilde{x}^2)\frac{\partial \tilde{y}}{\partial \tilde{x}}] + Pe^{i\frac{\omega}{\Omega}\tilde{t}} + S_c \tilde{y} \tag{4.18}$$

Applying the conversion to boundary conditions at the root in single beam model,

$$K_h \tilde{y} = -\lambda \frac{\partial^3 \tilde{y}}{\partial \tilde{x}^3} + \frac{1}{2}\frac{\partial \tilde{y}}{\partial \tilde{x}} \tag{4.19}$$

$$K_a \frac{\partial \tilde{y}}{\partial \tilde{x}} = \lambda \frac{\partial^2 \tilde{y}}{\partial \tilde{x}^2} \tag{4.20}$$

And at the tip,

$$\lambda \frac{\partial^2 \tilde{y}}{\partial \tilde{x}^2} = 0 \tag{4.21}$$

$$-\lambda \frac{\partial^3 \tilde{y}}{\partial \tilde{x}^3} = \frac{F_{point}}{\rho \Omega^2 L^2} \text{ or } 0 \tag{4.22}$$

Equation (4.18) ~ (4.22) are the full dimensionless mathematical description of single beam model.

3.6.2 MEMP Beam Model

In MEMP beam model, the conversion is more complicated.

$$\lambda_1 = \frac{E_1 I_1}{\rho_1 \Omega^2 L^4}, S_{c1} = \frac{S}{\rho_1 \Omega^2}, K_{h1} = \frac{k_h}{\rho_1 \Omega^2 L^2}, K_{a1} = \frac{k_a}{\rho_1 \Omega^2 L^3}, \tilde{\mu}_1 = \frac{\mu}{\rho_1 \Omega^2 L^2}, \tilde{\upsilon}_1 = \frac{\upsilon}{\rho_1 \Omega^2 L^2}$$
$$\lambda_2 = \frac{E_2 I_2}{\rho_2 \Omega^2 L^4}, S_{c2} = \frac{S}{\rho_2 \Omega^2}, K_{h2} = \frac{k_h}{\rho_2 \Omega^2 L^2}, K_{a2} = \frac{k_a}{\rho_2 \Omega^2 L^3}, \tilde{\mu}_2 = \frac{\mu}{\rho_2 \Omega^2 L^2}, \tilde{\upsilon}_2 = \frac{\upsilon}{\rho_2 \Omega^2 L^2}$$
$$P = \frac{p}{\rho_2 \Omega^2 L}$$

Applying the conversion to equation (4.9), it evolves to

$$\begin{aligned}
&\frac{\partial^2 \tilde{y}_1}{\partial \tilde{t}^2} = -\lambda_1 \frac{\partial^4 \tilde{y}_1}{\partial \tilde{x}^4} + \frac{1}{2}\frac{\partial}{\partial \tilde{x}}[(1-\tilde{x}^2)\frac{\partial \tilde{y}_1}{\partial \tilde{x}}] + \tilde{\mu}_1(\frac{\partial^2 \tilde{y}_1}{\partial \tilde{x}^2} - \frac{\partial^2 \tilde{y}_2}{\partial \tilde{x}^2}) \\
&+\tilde{\upsilon}_1(\frac{\partial^2 \tilde{y}_1}{\partial \tilde{x}^2} + \frac{\partial^2 \tilde{y}_2}{\partial \tilde{x}^2}) + S_{c1}(\tilde{y}_1 - \tilde{y}_2) \\
&\frac{\partial^2 \tilde{y}_2}{\partial \tilde{t}^2} = -\lambda_2 \frac{\partial^4 \tilde{y}_2}{\partial \tilde{x}^4} + \frac{1}{2}\frac{\partial}{\partial \tilde{x}}[(1-\tilde{x}^2)\frac{\partial \tilde{y}_2}{\partial \tilde{x}}] + \tilde{\mu}_2(\frac{\partial^2 \tilde{y}_2}{\partial \tilde{x}^2} - \frac{\partial^2 \tilde{y}_1}{\partial \tilde{x}^2}) \\
&+\tilde{\upsilon}_2(\frac{\partial^2 \tilde{y}_1}{\partial \tilde{x}^2} + \frac{\partial^2 \tilde{y}_2}{\partial \tilde{x}^2}) + S_{c2}(\tilde{y}_2 - \tilde{y}_1) + Pe^{i\frac{\omega}{\Omega}\tilde{t}}
\end{aligned} \tag{4.23}$$

Applying the conversion to boundary conditions at the root,

For the first beam (the spar),

$$K_{h1}\tilde{y}_1 = -\lambda_1 \frac{\partial^3 \tilde{y}_1}{\partial \tilde{x}^3} + \frac{1}{2}\frac{\partial \tilde{y}_1}{\partial \tilde{x}} + \tilde{\mu}_1\left(\frac{\partial^2 \tilde{y}_1}{\partial \tilde{x}^2} - \frac{\partial^2 \tilde{y}_2}{\partial \tilde{x}^2}\right) + \tilde{\upsilon}_1\left(\frac{\partial^2 \tilde{y}_1}{\partial \tilde{x}^2} + \frac{\partial^2 \tilde{y}_2}{\partial \tilde{x}^2}\right)$$
$$K_{a1}\frac{\partial \tilde{y}_1}{\partial \tilde{x}} - \lambda_1 \frac{\partial^2 \tilde{y}_1}{\partial \tilde{x}^2} = 0 \tag{4.24}$$

For the second beam (the shell),

$$K_{h2}\tilde{y}_2 = -\lambda_2 \frac{\partial^3 \tilde{y}_2}{\partial \tilde{x}^3} + \frac{1}{2}\frac{\partial \tilde{y}_2}{\partial \tilde{x}} + \tilde{\mu}_2\left(\frac{\partial^2 \tilde{y}_2}{\partial \tilde{x}^2} - \frac{\partial^2 \tilde{y}_1}{\partial \tilde{x}^2}\right) + \tilde{\upsilon}_2\left(\frac{\partial^2 \tilde{y}_1}{\partial \tilde{x}^2} + \frac{\partial^2 \tilde{y}_2}{\partial \tilde{x}^2}\right)$$
$$K_{a2}\frac{\partial \tilde{y}_2}{\partial \tilde{x}} - \lambda_2 \frac{\partial^2 \tilde{y}_2}{\partial \tilde{x}^2} = 0 \tag{4.25}$$

At the tip, for the first beam (the spar)

$$-\lambda_1 \frac{\partial^3 \tilde{y}_1}{\partial \tilde{x}^3} + \tilde{\mu}_1\left(\frac{\partial^2 \tilde{y}_1}{\partial \tilde{x}^2} - \frac{\partial^2 \tilde{y}_2}{\partial \tilde{x}^2}\right) + \tilde{\upsilon}_1\left(\frac{\partial^2 \tilde{y}_1}{\partial \tilde{x}^2} + \frac{\partial^2 \tilde{y}_2}{\partial \tilde{x}^2}\right) = 0$$
$$-\lambda_1 \frac{\partial^2 \tilde{y}_1}{\partial \tilde{x}^2} = 0 \tag{4.26}$$

For the second beam (the shell),

$$-\lambda_2 \frac{\partial^3 \tilde{y}_2}{\partial \tilde{x}^3} + \tilde{\mu}_2\left(\frac{\partial^2 \tilde{y}_2}{\partial \tilde{x}^2} - \frac{\partial^2 \tilde{y}_1}{\partial \tilde{x}^2}\right) + \tilde{\upsilon}_2\left(\frac{\partial^2 \tilde{y}_1}{\partial \tilde{x}^2} + \frac{\partial^2 \tilde{y}_2}{\partial \tilde{x}^2}\right) = \frac{F_{point}}{\rho_2 \Omega^2 L^2}$$
$$-\lambda_2 \frac{\partial^2 \tilde{y}_2}{\partial \tilde{x}^2} = 0 \tag{4.27}$$

Equations (4.23) ~ (4.27) are the full dimensionless mathematical description of MEMP beam model.

3.7 Variable Separation for Harmonic Excitation

Variable separation further simplifies the equations to be solved. In both single beam model and MEMP beam model, the governing equations have two variables: time t and deflection y. Assume that the dimensional solution to harmonic excitation ($p(x)e^{i\omega t}$ or $P(\tilde{x})e^{i\frac{\omega}{\Omega}\tilde{t}}$) has the following form,

$$y(x,t) = h(x)e^{i\omega t} \tag{4.28}$$

where

h - Deflection amplitude

ω - Harmonic excitation frequency

Apply the nondimentional conversion,

$$\tilde{y}(\tilde{x},\tilde{t}) = \tilde{h}(\tilde{x})e^{i\frac{\omega}{\Omega}\tilde{t}} \tag{4.29}$$

$\tilde{h}$ - Nondimensional deflection amplitude, $\frac{h}{L}$

For single beam model, substitute (4.29) into (4.18) and leave out $e^{i\frac{\omega}{\Omega}\tilde{t}}$,

$$-(\frac{\omega}{\Omega})^2\tilde{h}(x) = -\lambda\frac{\partial^4\tilde{h}(x)}{\partial\tilde{x}^4} + \frac{1}{2}\frac{\partial}{\partial\tilde{x}}[(1-\tilde{x}^2)\frac{\partial\tilde{h}(x)}{\partial\tilde{x}}] + P + S_c\tilde{h}(x)$$

Move all terms to one side,

$$(\frac{\omega}{\Omega})^2\tilde{h}(x) - \lambda\frac{\partial^4\tilde{h}(x)}{\partial\tilde{x}^4} + \frac{1}{2}\frac{\partial}{\partial\tilde{x}}[(1-\tilde{x}^2)\frac{\partial\tilde{h}(x)}{\partial\tilde{x}}] + P + S_c\tilde{h}(x) = 0 \tag{4.30}$$

For MEMP beam model, substitute (4.29) into (4.23) and leave out $e^{i\frac{\omega}{\Omega}\tilde{t}}$. For simplicity, the argument of $\tilde{h}(x)$ is omitted.

$$
\begin{aligned}
&(\frac{\omega}{\Omega})^2\tilde{h}_1-\lambda_1\frac{\partial^4\tilde{h}_1}{\partial\tilde{x}^4}+\frac{1}{2}\frac{\partial}{\partial\tilde{x}}[(1-\tilde{x}^2)\frac{\partial\tilde{h}_1}{\partial\tilde{x}}]+\tilde{\mu}_1(\frac{\partial^2\tilde{h}_1}{\partial\tilde{x}^2}-\frac{\partial^2\tilde{h}_2}{\partial\tilde{x}^2})\\
&+\tilde{\upsilon}_1(\frac{\partial^2\tilde{h}_1}{\partial\tilde{x}^2}+\frac{\partial^2\tilde{h}_2}{\partial\tilde{x}^2})+S_{c1}(\tilde{h}_1-\tilde{h}_2)=0\\
&(\frac{\omega}{\Omega})^2\tilde{h}_2-\lambda_2\frac{\partial^4\tilde{h}_2}{\partial\tilde{x}^4}+\frac{1}{2}\frac{\partial}{\partial\tilde{x}}[(1-\tilde{x}^2)\frac{\partial\tilde{h}_2}{\partial\tilde{x}}]+\tilde{\mu}_2(\frac{\partial^2\tilde{h}_2}{\partial\tilde{x}^2}-\frac{\partial^2\tilde{h}_1}{\partial\tilde{x}^2})\\
&+\tilde{\upsilon}_2(\frac{\partial^2\tilde{h}_1}{\partial\tilde{x}^2}+\frac{\partial^2\tilde{h}_2}{\partial\tilde{x}^2})+S_{c2}(\tilde{h}_2-\tilde{h}_1)+P=0
\end{aligned}
\tag{4.31}
$$

The variable separation for boundary conditions is also necessary but not listed here for simplicity. Equation (4.30), (4.31) combined with all separated boundary conditions constitutes the full sets of mathematical description that are ready to be solved numerically for both models. The next chapter will provide the details of this process.

4 Computer Modeling

The goal of computer modeling is to numerically solve the solution of two models. There are a number of numerical methods that can achieve this. Three widely used methods are listed below.

1. Finite difference method

2. Finite element method

3. Power series method

Although the first two methods are efficient and accurate, from the point of ease of analysis, power series method is used. The basic concept of this method is to express the deflection y as a power series which is truncated at certain order. If this truncated power series satisfied equation (4.18) or (4.23) and the associated boundary conditions, it can be considered as an estimation of the true solution. This thesis uses Wolfram Mathematica to develop the computer code, which is included in appendix B.

4.1 Algorithm

For single beam model, the algorithm of the code can be divided into five parts.

(1) Assume that $\tilde{h} = \sum_{k=0}^{n-1} a_k \tilde{x}^k$, where n is the truncation number which indicates how many terms will be used to estimate the solution. The larger this number is, the more accurate the result will be.

(2) Substitute $\tilde{h} = \sum_{k=0}^{n-1} a_k \tilde{x}^k$ into equation (30) and group the coefficients for each order of x. Equation (30) becomes

$$\sum_{k=0}^{n-1} Coeff_k(non\dim ensional\ \ parameters, a_0 \cdots a_{n-1}) x^k = 0$$

Since x is arbitrary, all coefficients must equal to zero.

$$\left.\begin{array}{l} Coeff_0(non\dim ensional\ \ parameters, a_0 \cdots a_{n-1}) = 0 \\ \quad \vdots \\ Coeff_{n-1}(non\dim ensional\ \ parameters, a_0 \cdots a_{n-1}) = 0 \end{array}\right\} n\ equations$$

(3) Substitute $\tilde{h} = \sum_{k=0}^{n-1} a_k \tilde{x}^k$ and the boundary value of x into four boundary conditions.

$$\left.\begin{array}{l} BC_1(non\dim ensional\ \ parameters, a_0 \cdots a_{n-1}) = 0 \\ BC_2(non\dim ensional\ \ parameters, a_0 \cdots a_{n-1}) = 0 \\ BC_3(non\dim ensional\ \ parameters, a_0 \cdots a_{n-1}) = 0 \\ BC_4(non\dim ensional\ \ parameters, a_0 \cdots a_{n-1}) = 0 \end{array}\right\} 4\ equations$$

(4) Since the power series $\tilde{h} = \sum_{k=0}^{n-1} a_k \tilde{x}^k$ is truncated and the highest order of derivative in equation (30) is four, the coefficients of the first four highest x powers ($x^{n-1}, x^{n-2}, x^{n-3}, x^{n-4}$) are incomplete. Thus only (n-4) equations in step (2) are valid. Plus the four boundary condition equations, there are n equations in total.

$$\left.\begin{array}{l}\left.\begin{array}{l} Coeff_0(non\dim ensional\ \ parameters, a_0 \cdots a_{n-1}) = 0 \\ \vdots \\ Coeff_{n-5}(non\dim ensional\ \ parameters, a_0 \cdots a_{n-5}) = 0 \end{array}\right\} (n-4)\ equations \\ \left.\begin{array}{l} BC_1(non\dim ensional\ \ parameters, a_0 \cdots a_{n-1}) = 0 \\ BC_2(non\dim ensional\ \ parameters, a_0 \cdots a_{n-1}) = 0 \\ BC_3(non\dim ensional\ \ parameters, a_0 \cdots a_{n-1}) = 0 \\ BC_4(non\dim ensional\ \ parameters, a_0 \cdots a_{n-1}) = 0 \end{array}\right\} 4\ equations \end{array}\right\} n\ equations$$

(5) These n equations contain n unknowns ($a_0 \ldots a_{n-1}$). The unique solutions for them can be solved.

The following diagram shows the algorithm.

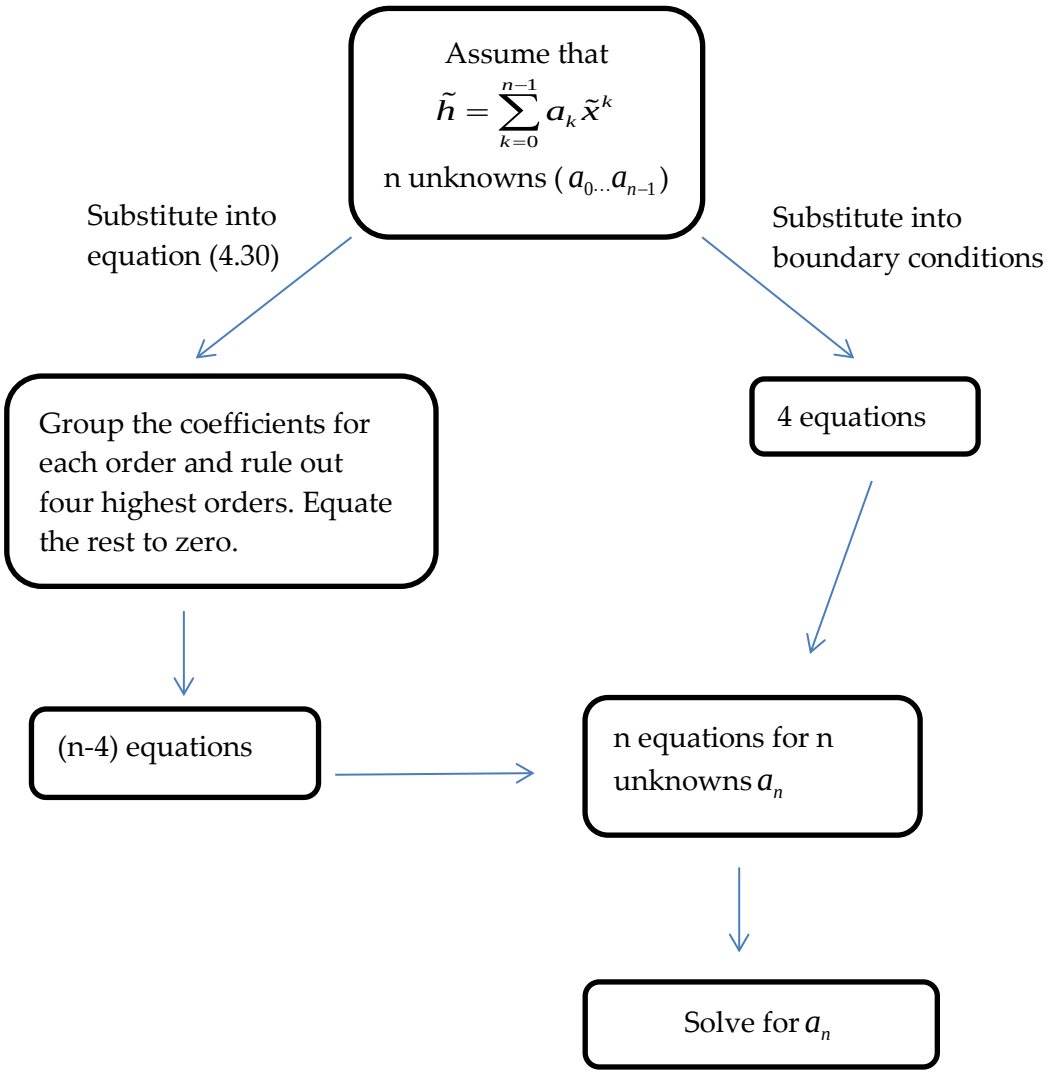

Figure 16: Single beam model algorithm

For MEMP beam model, the process is almost the same except for the fact that there are n more equations and n more unknowns. The following diagram illustrates the algorithm.

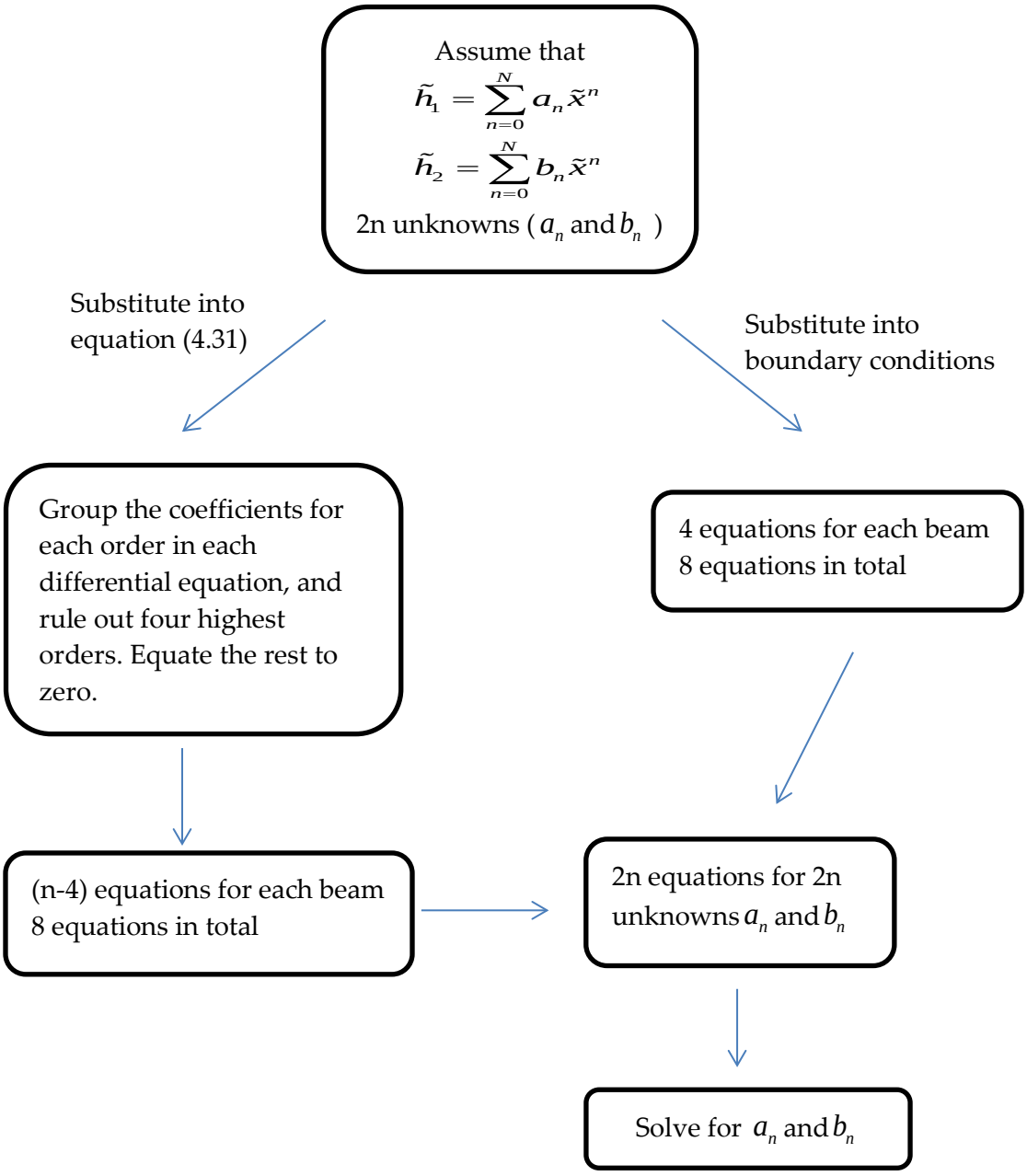

Figure 17: MEMP beam model algorithm

4.2 Aerodynamic Force Input

As discussed in previous chapter, the aerodynamic forces in these two models are position dependent harmonics. In mathematics, any periodic function can be decomposed to a series of harmonics using Fourier expansion. In reality, although the aerodynamic force is not pure harmonic, they are periodic, so composed of harmonics.

$$f_{aero}(x,t) = a_0 + \sum_n (a_n \cos(n\omega_0 t) + b_n \sin(n\omega_0 t))$$

where ω_0 - Fundamental frequency.

a_0 - Static aerodynamic force

Many experiments have been done to study the aerodynamic forces on helicopter blades. Among them, J. P. Rabbott, Jr and others (U. S. army aviation materiel laboratories, 1966) obtained the first ten harmonics of the aerodynamic force on CH 34 helicopter. In this thesis, all these ten harmonics are described as polynomials of certain order, which are included in Appendix A. This description is consistent with the power series solution method for the governing equations. Figure 18 and Figure 19 show the first and second cosine and sine harmonics.

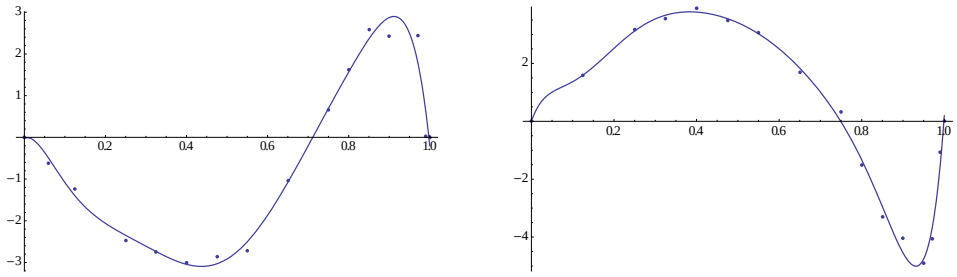

Figure 18: First sine and cosine harmonics. X axis: radial position. Y axis: aerodynamic force (lb/in)

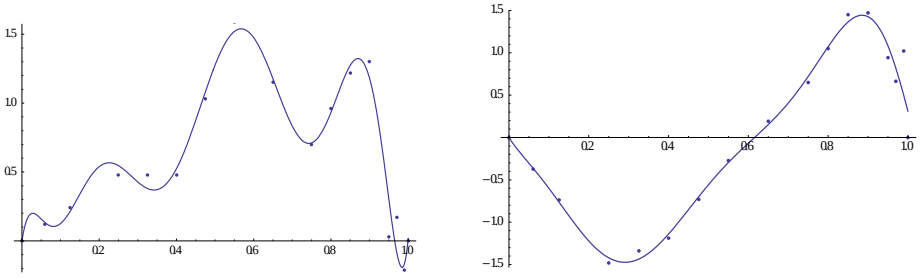

Figure 19: Second sine and cosine harmonics. X axis: radial position. Y axis: aerodynamic force (lb/in)

4.3 Solution

This section introduces the relation between single beam model and MEMP beam model, and several key numerical quantities.

4.3.1 Conversion from MEMP beam to single beam

In the course of this work, all the numerical results of single beam model are transferred from MEMP beam model. As discussed previously, a MEMP model with a very strong spring between the shell and the spar behaves the same as the single beam

model because the rigid connection makes the shell and the spar move together. That is, the deflection, the hub loads and the transfer function are exactly the same. Since the computer code for MEMP beam model is able to give results for both single and MEMP beam model, there is no need to keep the program specific for single beam model. The computer codes discussed afterwards are all considered as MEMP model code otherwise specified.

4.3.2 Deflection

Once the aerodynamic force input is determined, the computer code shown in section 4.1 is able to solve the unknowns a_n and b_n. Then, the deflections are given below,

$$\tilde{y}_1 = \tilde{h}_1 e^{i\frac{w}{\Omega}\tilde{t}} = (\sum_{n=0}^{N} a_n \tilde{x}^n) e^{i\frac{w}{\Omega}\tilde{t}}$$

$$\tilde{y}_2 = \tilde{h}_2 e^{i\frac{w}{\Omega}\tilde{t}} = (\sum_{n=0}^{N} b_n \tilde{x}^n) e^{i\frac{w}{\Omega}\tilde{t}}$$

These are the nondimensional deflections for the spar and shell in MEMP beam model. The relative deflection of these two is equals to,

$$\Delta y = \tilde{y}_1 - \tilde{y}_2 = (\tilde{h}_1 - \tilde{h}_2) e^{i\frac{w}{\Omega}\tilde{t}} = \sum_{n=0}^{N} (a_n - b_n) \tilde{x}^n e^{i\frac{w}{\Omega}\tilde{t}}$$

It turns out this is a very import quantity used to assess the MEMP design.

For single beam model, there is only one deflection.

$$\tilde{y} = \tilde{h}e^{i\frac{w}{\Omega}\tilde{t}} = (\sum_{n=0}^{N} a_n \tilde{x}^n)e^{i\frac{w}{\Omega}\tilde{t}}$$

4.3.3 Hub Load Transfer Function in Frequency Domain

Another very important quantity is the hub load transfer function. It is defined as the absolute value of ratio of hub force to the total aerodynamic force along the beam.

$$hub\ load\ transfer\ \ function = |\frac{\tilde{F}_{hub}}{\sum aerodynamic\ \ force}|$$

In MEMP model, the hub load comes from two beams' boundary springs.

$$\tilde{F}_{hub} = K_{h1}\tilde{y}_1\big|_{root} + K_{h2}\tilde{y}_2\big|_{root} = (K_{h1}\sum_{n=0}^{N} a_n \tilde{x}^n\Big|_{root} + K_{h2}\sum_{n=0}^{N} b_n \tilde{x}^n\Big|_{root})e^{i\frac{w}{\Omega}\tilde{t}}$$

And $\sum aerodynamic\ \ force = (\int_{root}^{tip} Pdx)e^{i\omega t}$

Thus,

$$hub\ load\ transfer\ \ function = |\frac{(K_{h1}\sum_{n=0}^{N} a_n \tilde{x}^n\Big|_{root} + K_{h2}\sum_{n=0}^{N} b_n \tilde{x}^n\Big|_{root})e^{i\frac{w}{\Omega}\tilde{t}}}{(\int_{root}^{tip} Pdx)e^{i\omega t}}|$$

$$= |\frac{K_{h1}\sum_{n=0}^{N} a_n \tilde{x}^n\Big|_{root} + K_{h2}\sum_{n=0}^{N} b_n \tilde{x}^n\Big|_{root}}{\int_{root}^{tip} Pdx}|$$

Recall equation (4.31). The numerical solution of a_n *and* b_n are dependent on harmonic excitation frequency ω. Therefore, hub load transfer function is also dependent on ω. Figure 18 gives a plot of hub load transfer function in frequency domain.

For single beam model, the hub load only comes from one beam.

$$hub\ load\ transfer\ \ function == \frac{K_h \sum_{n=0}^{N} a_n \tilde{x}^n \Big|_{root}}{\int_{root}^{tip} Pdx}$$

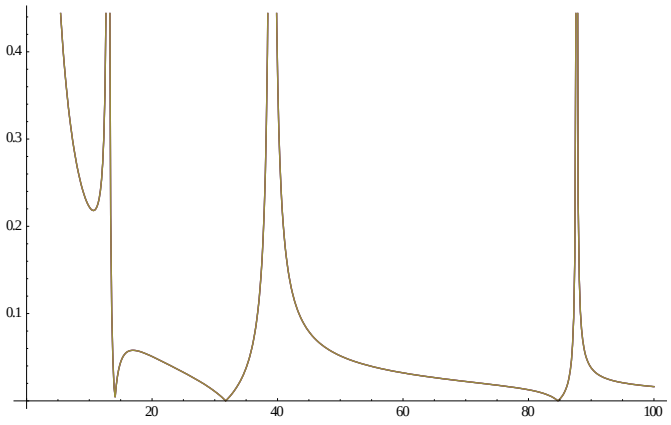

Figure 20: Hub load transfer function. X axis: frequency. Y axis: hub load transfer function.

4.3.4 Total Hub Load in Time Domain

The hub load is given in prior section for MEMP beam model.

$$\tilde{F}_{hub} = K_{h1}\,\tilde{y}_1\big|_{root} + K_{h2}\,\tilde{y}_2\big|_{root} = (K_{h1}\sum_{n=0}^{N} a_n\,\tilde{x}^n\Big|_{root} + K_{h2}\sum_{n=0}^{N} b_n\,\tilde{x}^n\Big|_{root})e^{i\frac{w}{\Omega}\tilde{t}}$$

This hub load is frequency dependent. In other words, if the frequency is fixed, this hub load is the response from a single frequency. As discussed before, the aerodynamic force applied on the rotor blade is not a single harmonic but can be decomposed into a sum of harmonics. If all the hub loads from those harmonics are added together, the total hub loads responsible for this aerodynamic force is obtained due to the linearity of equation (4.31). Therefore,

$$Total\ Hub\ Loads = \sum_{k} \tilde{F}_{hub}^{kth\ harmonic}$$

Because the frequencies are fixed in above expression, the total hub loads is only a function of time. Obviously, the bigger the k is, the more accurate the total hub loads can be. In this thesis, k equals to 10. Figure 21 below shows an example of total hub loads in time domain.

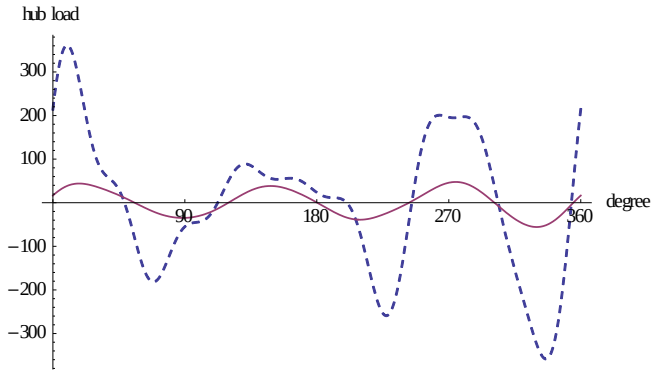

Figure 21: Total hub loads in time domain. X axis: time in one period. Y axis: hub load transfer function.

4.3 Numerical Convergence and Solution Verification

To ensure the numerical solution is correct, it is necessary to check the convergence of the solution. This can be done by comparing the numerical results with two successive truncation numbers. If the relative change is less than 10^{-5}, the solution is considered as convergent. A number of experiments have been done to test what is a proper value for the truncation number and the results show n = 100 is good enough, at which the program run time for calculating hub load is less than 3 minutes in frequency domain and less than 30 seconds in time domain.

Another fact that needs to be verified is the numerical solution converges to the true solution. This fact can be investigated both mathematically and physically. The behavior of the MEMP beam would be the same as that of a single beam if the springs between the shell and spar are very strong. Thus, by checking the consistency between these two cases, the numerical solution can be verified. Another quick test to the correctness of numerical solution is to calculate the hub load transfer function under the static aerodynamic force and see if the result equals to one, because for a static case, the hub load must equal to the total aerodynamic force.

5. Results from Models

This chapter presents the results for two models during the course of this work.

5.1 Data Input

This thesis uses parameters of CH-34 helicopter to run experiments. The main parameters include the geometry of rotor blades, the material properties, the rotation speed, the aerodynamic force, etc. They are listed below.

Table 1: Key parameters from CH -34 helicopters

Blade Radius – L	28 feet	Blade Mass - ρ	0.205 slug/feet
Rotation speed - Ω	23 rad/sec	Blade Bending stiffness - EI	102000 lb-ft^2
advance ratio	0.29	Hinge Point	1.4 feet

The dimensional parameters listed above cannot be used in computer model until they are converted to nondimensional parameters. Table 2 gives all nondimensional parameters required in computer model.

Table 2: Data Input

Oder of polynomial - N	0 ~ 100
Spar spring stiffness - S_{c1}	$S_{c1} = \frac{S}{\rho_1 \Omega^2}$
Shell spring stiffness - S_{c2}	$S_{c2} = \frac{S}{\rho_2 \Omega^2}$
Spar bending stiffness - λ_1	$\lambda_1 = \frac{E_1 I_1}{\rho_1 \Omega^2 L^4}$
Shell bending stiffness - λ_2	$\lambda_2 = \frac{E_2 I_2}{\rho_2 \Omega^2 L^4}$
Spar torsional spring stiffness of the first kind- $\tilde{\mu}_1$	$\tilde{\mu}_1 = \frac{\mu}{\rho_1 \Omega^2 L^2}$
Shell torsional spring stiffness of the first kind - $\tilde{\mu}_2$	$\tilde{\mu}_2 = \frac{\mu}{\rho_2 \Omega^2 L^2}$
Spar torsional spring stiffness of the second kind - $\tilde{\upsilon}_1$	$\tilde{\upsilon}_1 = \frac{\upsilon}{\rho_1 \Omega^2 L^2}$
Shell torsional spring stiffness of the second kind - $\tilde{\upsilon}_2$	$\tilde{\upsilon}_2 = \frac{\upsilon}{\rho_2 \Omega^2 L^2}$
nondimensional frequency square	$(\frac{\Omega}{\omega})^2$
nondimensional distributed aerodynamic force - P	$P = \frac{p}{\rho_2 \Omega^2 L}$
nondimensional point aerodynamic force - F	$F = \frac{f}{\rho_2 \Omega^2 L^2}$
Spar boundary spring stiffness - K_{h1}	$K_{h1} = \frac{k_h}{\rho_1 \Omega^2 L^2}$
Spar boundary torsional spring stiffness - K_{a1}	$K_{a1} = \frac{k_a}{\rho_1 \Omega^2 L^3}$
Shell boundary spring stiffness - K_{h2}	$K_{h2} = \frac{k_h}{\rho_2 \Omega^2 L^2}$
Shell boundary torsional spring stiffness - K_{a2}	$K_{a2} = \frac{k_a}{\rho_2 \Omega^2 L^3}$

Table 2 contains sixteen nondimensional parameters. One objective of this thesis is to explore the optimal combination of these parameters such that the MEMP design has enough vibration reduction while maintains necessary static strength and acceptable deflection.

5.2 Hub Load Transfer Function in Frequency Domain

The blade vibration due to aerodynamic force will spread to the rotor hub, leading the unwanted vibration further propagates into fuselage. The objective of applying MEMP design to rotor blade is to reduce this hub vibration, therefore attenuate the vibration on fuselage. As discussed above, the absolute value of ratio of the hub force to the total aerodynamic force applied on the blade is defined as the hub load transfer function. It can be considered as a measurement of vibration reduction.

5.2.1 Parametric Study

Since there are sixteen nondimensional parameters that can affect the hub load transfer function, it is necessary to perform parametric study first. Several important parameters are discussed in detail below.

(1) Spring between shell and spar

The most influential factor to hub load transfer function in frequency domain is the springs between the shell and the spar, which appears in the nondimensional parameters S_{c1} and S_{c2}. Figure 22 shows three hub load transfer functions in frequency domain with different springs. The smooth curve has the highest spring stiffness while the dashed curve has the lowest one. The differences between these three cases indicate that the higher spring stiffness results in a higher hub load transfer function and vice versa.

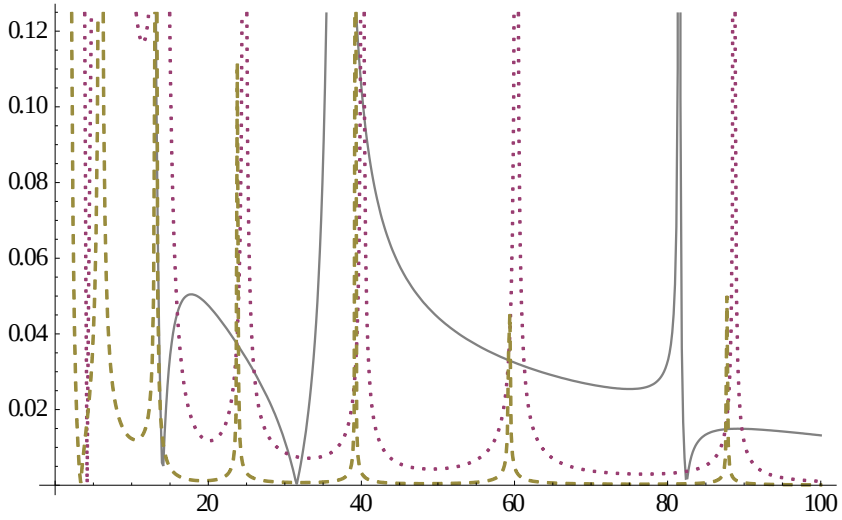

Figure 22: Hub load transfer function with different spring stiffness. X axis: $(\frac{\omega}{\Omega})^2$. Y axis: Hub load transfer function

Apart from the stiffness, the radial distribution of the spring, now $S(x)$, also influences the hub load transfer function. Figure 23 illustrates this behavior. The dotted curve represents the uniform distribution of spring with average stiffness of one. The

dashed curve, however, represents the triangular distribution of spring with the same average stiffness. We see these two hub load transfer functions are close in the plot at higher frequency but different at lower frequency. That means the distribution of spring does not have a significant influence on higher frequency vibration reduction but leads more hub load for lower frequency. This characteristic will be used later to reduce the MEMP beam deflection without much compromise on vibration reduction.

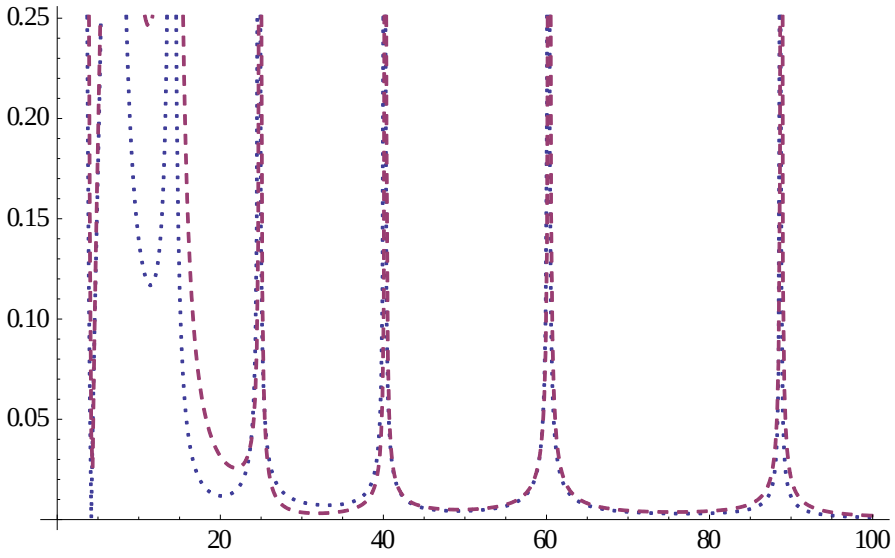

Figure 23: Hub load transfer function with different spring stiffness distribution. X axis: $(\frac{\omega}{\Omega})^2$. Y axis: Hub load transfer function

(2) Torsional spring

The main effect of torsional spring is to maintain the static strength, which will be discussed later. But it has considerable influence on hub load transfer function, which is shown in the following figure.

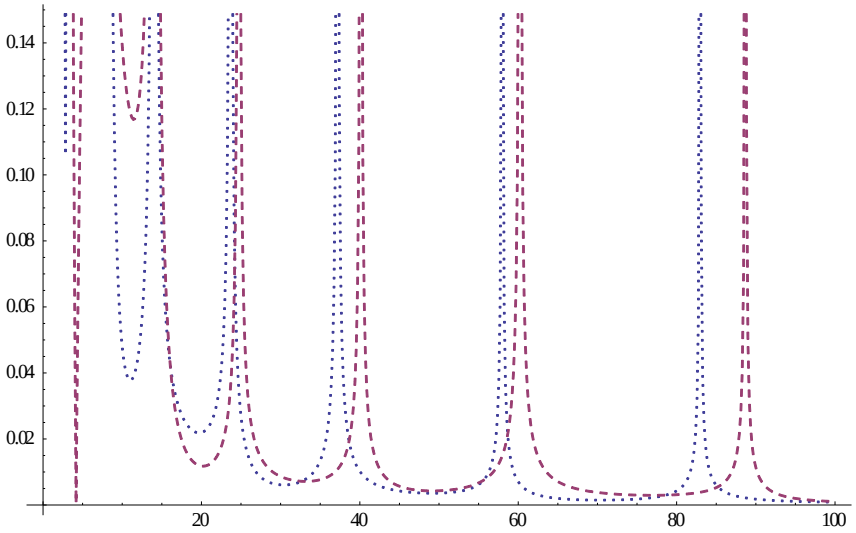

Figure 24: Hub load transfer function with different torsional springs. X axis: $(\frac{\omega}{\Omega})^2$. Y axis: Hub load transfer function

Figure 24 displays two hub load transfer functions with different torsional springs in frequency domain. In the figure, these two curves generally have the same vibration reduction but are shifted apart. As we know, the peak of the curves marks the natural frequency of the structure. Therefore, the torsional spring is able to alter the structure's natural frequency. This is a very important characteristic that will be used later. It serves as an effective approach to maintain the vibration reduction but decrease the deflection.

(3) Bending stiffness

The bending stiffness is another important quantity that affects the MEMP structure performance. Both bending stiffness (the spar and the shell) will change together in the following simulation.

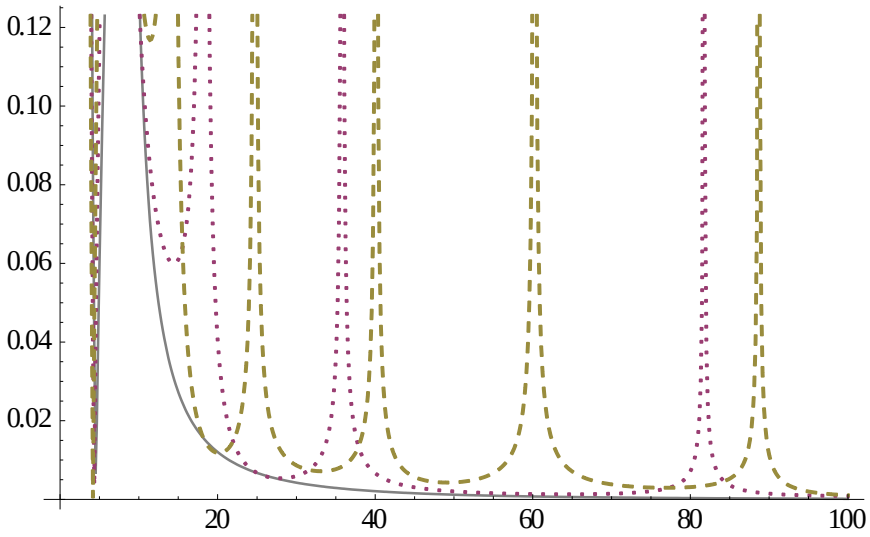

Figure 25: Hub load transfer function with different bending stiffness. X axis: $(\frac{\omega}{\Omega})^2$. Y axis: Hub load transfer function. Smooth curve: strong bending stiffness. Dotted curve: median bending stiffness. Dashed curve: soft bending stiffness.

Figure 25 shows three cases over the frequency domain. It can be seen that the case with stronger bending stiffness is likely to have fewer peaks. In other words, the strong bending stiffness results in sparse natural frequencies, which is the same as for a single beam model. These sparse natural frequencies will lower the possibility of the occurrence of resonance. Thus, in general, a MEMP structure with a strong bending stiffness is a desirable design in terms of reducing the potential vibration.

(4) Aerodynamic force

From mathematical view, because the system is linear the amplitude of aerodynamic force does not have an effect on hub load transfer function. However, the load distribution does matter. There are so many kinds of distributions that it is very difficult to have a thorough understanding for all of them. This section only studies the end point force and some simple continuous distributions.

Figure 26 illustrates three hub load transfer functions with different force distributions, which are listed in Figure 27. Note that the total force for these three distributions is the same.

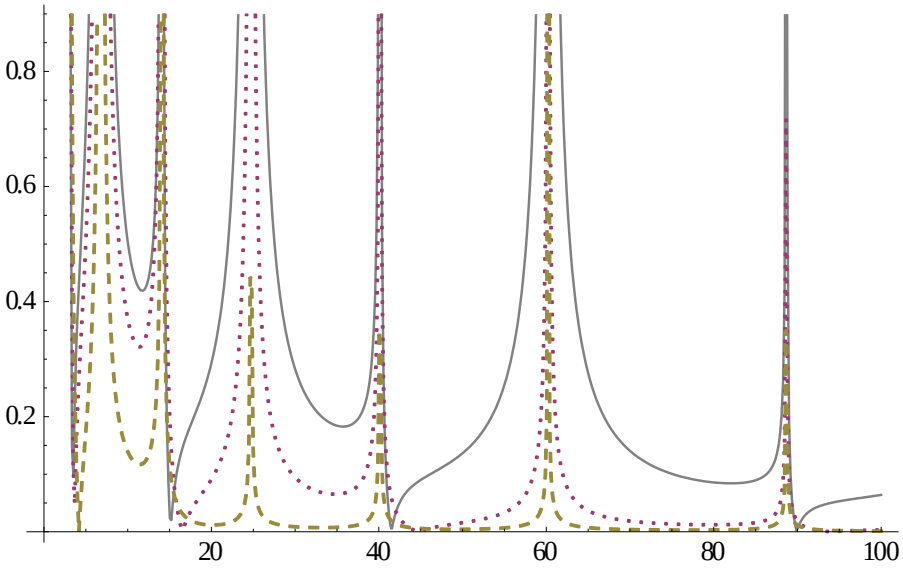

Figure 26: Hub load transfer function with different force distribution. X axis: $(\frac{\omega}{\Omega})^2$. Y axis: Hub load transfer function. See Figure 27 for Force distribution of three curves

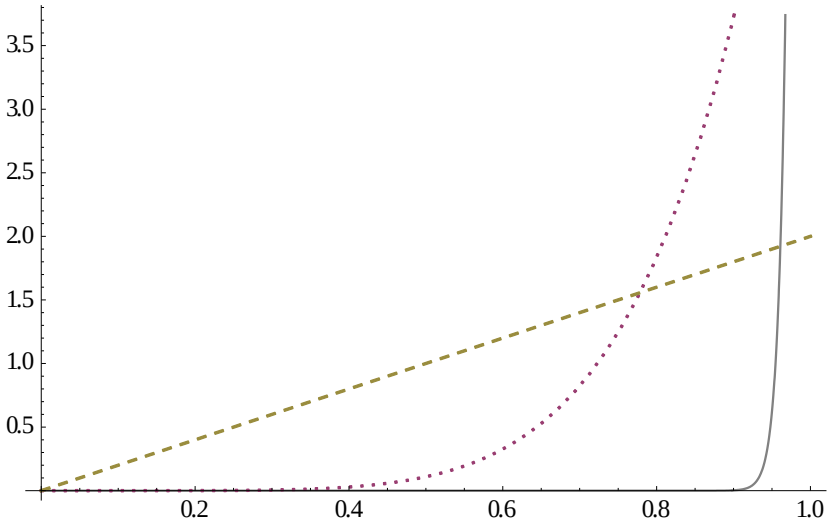

Figure 27: Aerodynamic force distribution. X axis: radial position. Y axis: nondimensional force

As can be seen, the hub response of the end point force is the most intense one. The triangular distributed force has the best vibration reduction. Although the average force is the same for these three forces, the response varies. In other words, the force distribution strongly affects the hub load. This conclusion may not help in the study of a helicopter rotor as all the aerodynamic forces are distributed along the whole blade, but it might apply to some other rotor studies where point force is the potential excitation.

(5) Boundary spring

The boundary spring is the connection between the beam and the hub, thus a critical component in rotor structure. In the MEMP model, there are four boundary springs: two linear boundary springs and two torsional boundary springs. This section

only studies the effect of linear springs. All torsional springs' stiffness is set to be zero simulating pinned connections. In order to avoid too much deflection, the spar's linear boundary spring is set to be very strong so that the spar can be considered as a pinned beam to the hub. The shell's linear boundary spring ranges from "zero" to "strong". Three examples are illustrated in Figure 28.

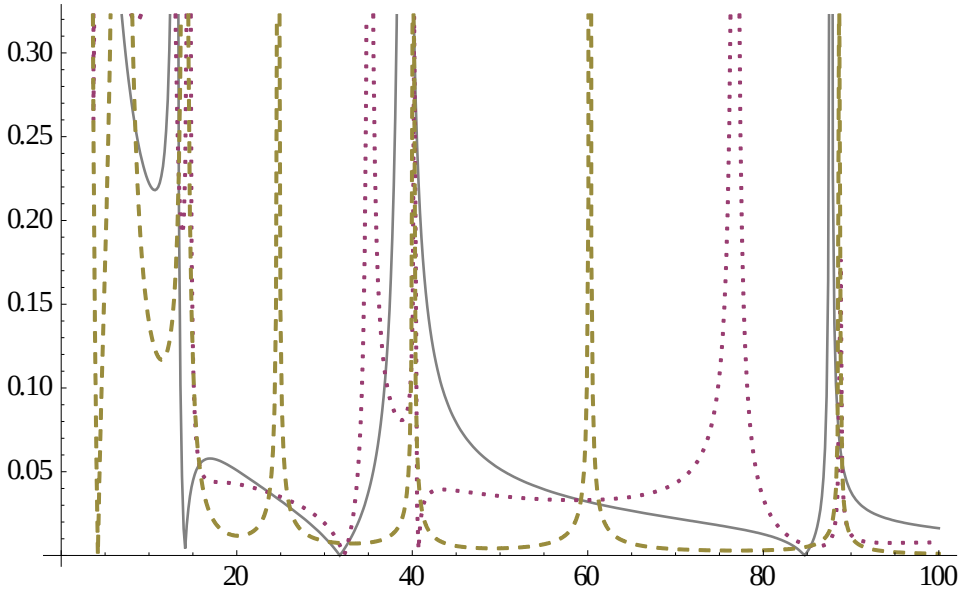

Figure 28: Hub load transfer function with different linear boundary spring. . X axis: $(\frac{\omega}{\Omega})^2$. Y axis: Hub load transfer function. Smooth curve: strong. Dotted curve: median. Dashed curve: zero

The results indicate that raising the linear boundary spring's stiffness will lead to a higher hub load transfer function. Therefore, in order to minimize the hub load, the stiffness of shell's linear boundary spring should be zero.

(6) Identical beams versus different beams

In the above parametric study, the shell and the spar are considered to have the same properties. However, some differences in properties can bring benefits to the MEMP design. Such differences include the different mass and different bending stiffness. They are discussed below.

Figure 29 and Figure 30 display three hub load transfer functions with different bending stiffness. We can see the case with a stiffer spar and a flexible shell has the best vibration reduction and the fewest peaks. This result confirms the previous theoretical and experimental work done by Professor Bliss at Duke University.

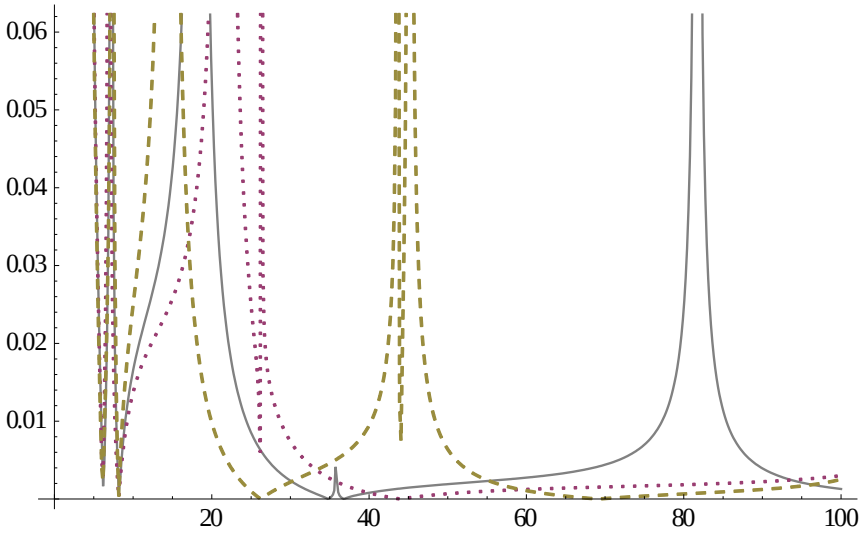

Figure 29: Hub load transfer function. X axis: $(\frac{\omega}{\Omega})^2$. Y axis: Hub load transfer function. Smooth curve: identical beams. Dotted curve: different beams with stiffer spar and flexible shell. Dashed curve: different beams with flexible spar and stiffer spar.

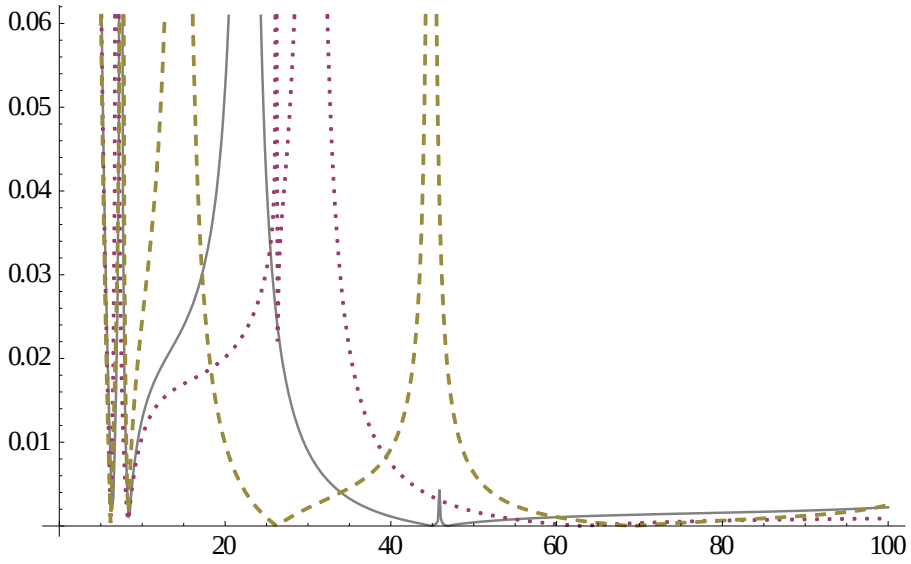

Figure 30: Hub load transfer function. X axis: $(\frac{\omega}{\Omega})^2$. Y axis: Hub load transfer function. Smooth curve: identical beams. Dotted curve: different beams with stiffer spar and flexible shell. Dashed curve: different beams with flexible spar and stiffer spar.

Figure 31 shows three hub load transfer functions with different beam masses, while the total mass remains constant. We can see they all have the same level of vibration reduction but with different natural frequencies. Since this change only affects the natural frequencies of the structure and does not sacrifice vibration reduction, the approach can be employed later to reduce the beam deflection.

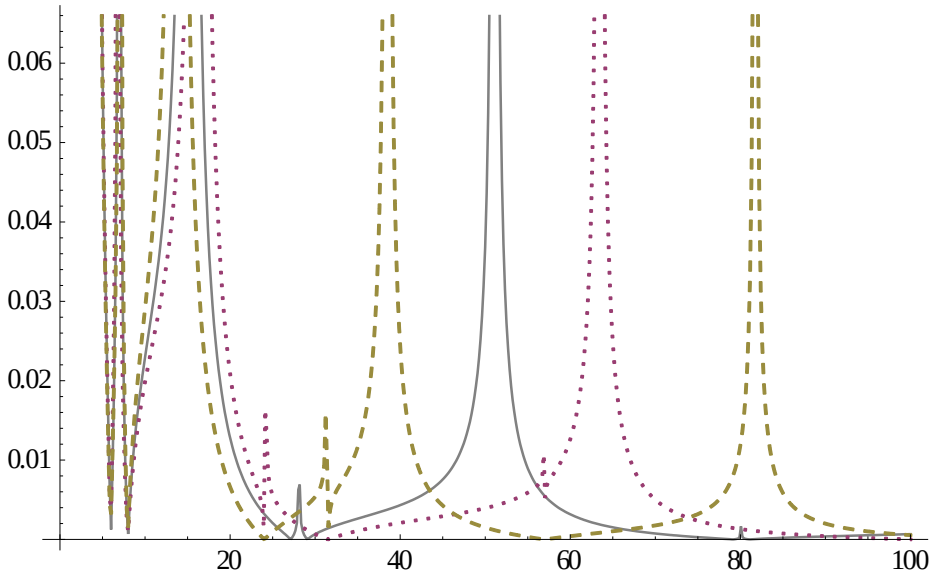

Figure 31: Hub load transfer function with different mass beams. X axis: $(\frac{\omega}{\Omega})^2$. Y axis: Hub load transfer function. Smooth curve: identical beams. Dotted curve: different beams with heavier spar and lighter shell. Dashed curve: different beams with lighter spar and heavier spar.

5.2.2 Comparison between Two Designs

The parametric study reveals some basic characteristics of hub load transfer function, which will benefit the MEMP design by maximizing its advantages. Based on these characteristics, this section compares the hub load transfer function of MEMP design (MEMP beam model) with that of traditional design (single beam model) in frequency domain to show the benefits of applying MEMP design.

The comparison is based on the same average mass, same average bending stiffness and same aerodynamic force distribution for both models. As discussed in a

previous chapter, to simulate the behavior of single beam, the spring stiffness between the shell and the spar in computer model needs to be very strong.

Figure 32 shows four cases with different spring stiffness. The Smooth curve is considered as the single beam. As can be seen, the last two MEMP beams' vibration reductions are much better than the single beam. This result gives a promising future of applying MEMP design to achieve rotor hub vibration reduction.

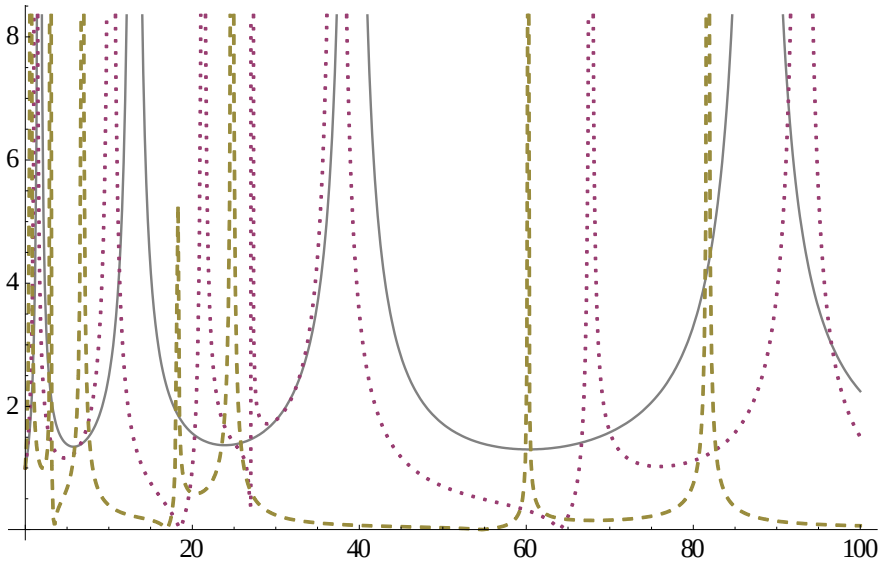

Figure 32: Hub load transfer function. Smooth curve: single beam. X axis: $(\frac{\omega}{\Omega})^2$. Y axis: Hub load transfer function. Dotted curve: MEMP beam with strong spring stiffness. Dashed curve: MEMP beam with median spring stiffness.

The result shown above is the response of end point aerodynamic force. For distributed aerodynamic force, Figure 33 gives an example. The aerodynamic force in this experiment is evenly distributed along the blade. Apparently, the same conclusion

can be drawn from Figure 33. The MEMP beam has a much better vibration reduction performance than a single beam.

Both Figure 32 and Figure 33 list the normal cases of single beam and MEMP beam. The hub loads of these two kinds of design are distinct. Based on the conclusion from last section, the vibration reduction performance can be even improved by properly setting up some parameters, such as the boundary springs, the mass and the stiffness of each beam and the overall bending stiffness. However, in the real world, some assumptions may not be true and some restrictions may apply on these two models. The purpose of section 5.2 is to present a general idea that MEMP design may have the practical use and how it can be adjusted in the real world.

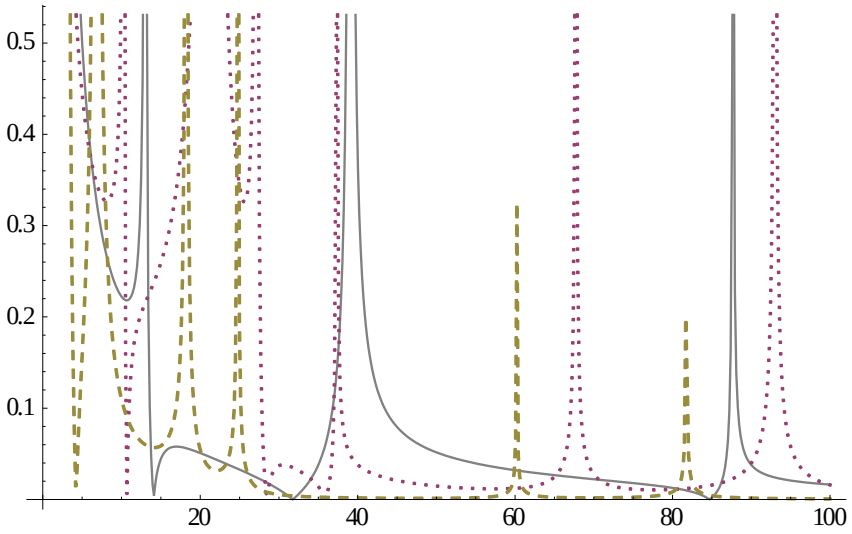

Figure 33: Hub load transfer function. X axis: $(\frac{\omega}{\Omega})^2$. Y axis: Hub load transfer function. Smooth curve: single beam. Dotted curve: MEMP beam with strong spring stiffness. Dashed curve: MEMP beam with soft spring stiffness.

5.3 Hub Loads in Time Domain

5.3.1 Introduction

As discussed in chapter 5, a periodic aerodynamic force can be expressed as the following form,

$$f_{aero}(x,t) = a_0 + \sum_n (a_n \cos(n\omega_0 t) + b_n \sin(n\omega_0 t))$$

ω_0 - Fundamental frequency

Unlike the above cases, the aerodynamic force is no longer a harmonic force but consists of different frequency components ($\omega = n\Omega$). It is inconvenient to show its response on a frequency domain. Instead, the response in time domain can provide a clearer understanding. As stated previously, the first ten harmonics of CH-34 rotor blade's aerodynamic force are described by polynomials in Appendix A. Figure 34 shows the time history of such aerodynamic force at radial position 0.25R.

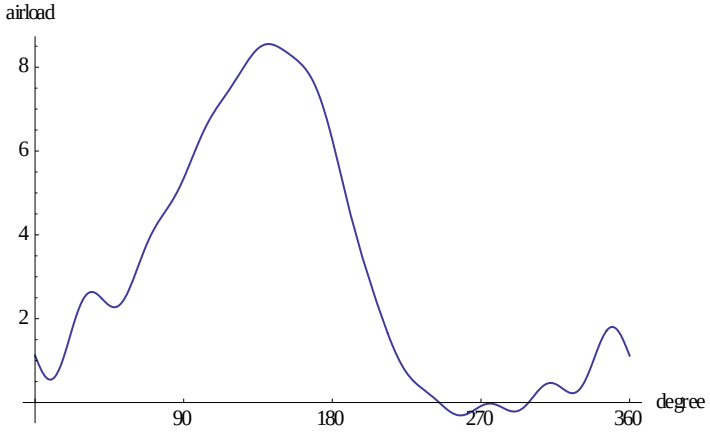

Figure 34: Aerodynamic force at 0.25R in time domain. X axis: azimuthal angle in degrees. Y axis: aerodynamic force (lb/in)

As can be seen, the variation of aerodynamic force in one period is large. At some point, it is even negative. This is due to the high advance ratio of the helicopter.

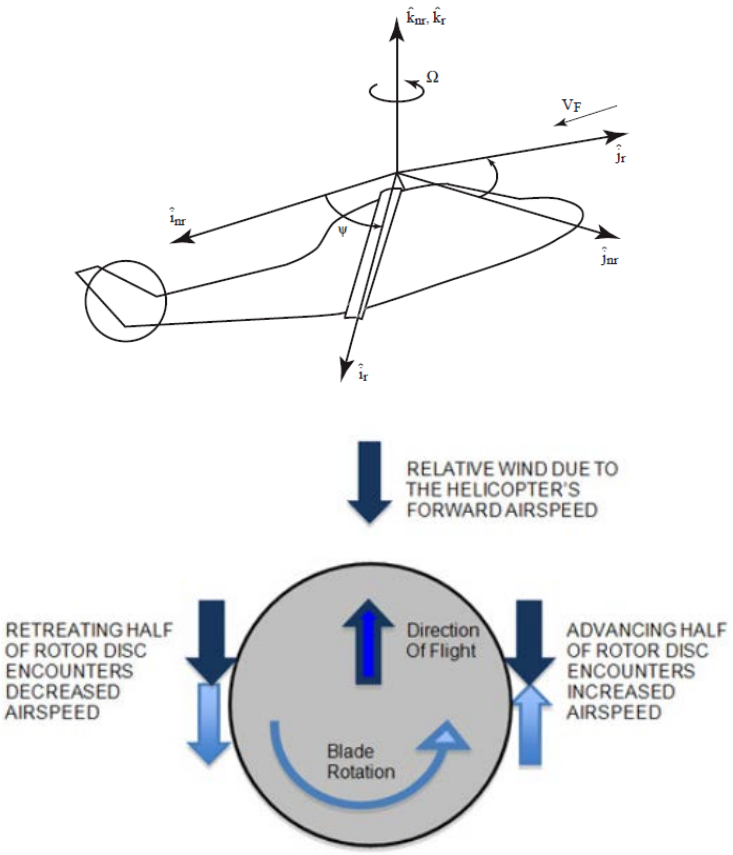

Figure 35: Helicopter blade speed while flying forward.

Figure 35 shows the rotor blade speed while a helicopter is flying forward. It can be seen, when a rotor blade runs one revolution, it undergoes different airspeed. This fact causes large variation in blade aerodynamic force. The 0^{th} harmonic of aerodynamic

force, which is called the static airload and denoted as a_0 in the formula, is the force that holds the helicopter up. The rest harmonics are called the dynamic airload because they are time dependent. Among dynamic airload, the first and second harmonics are lower harmonic airload, which are proven to be canceled at the hub due to the symmetric structure of helicopter rotor. The rest dynamic airload, which is called higher harmonic airload, especially the 3rd, 4th and 5th, and beyond, creates the unwanted hub vibration. The following diagram shows the relations for different airload.

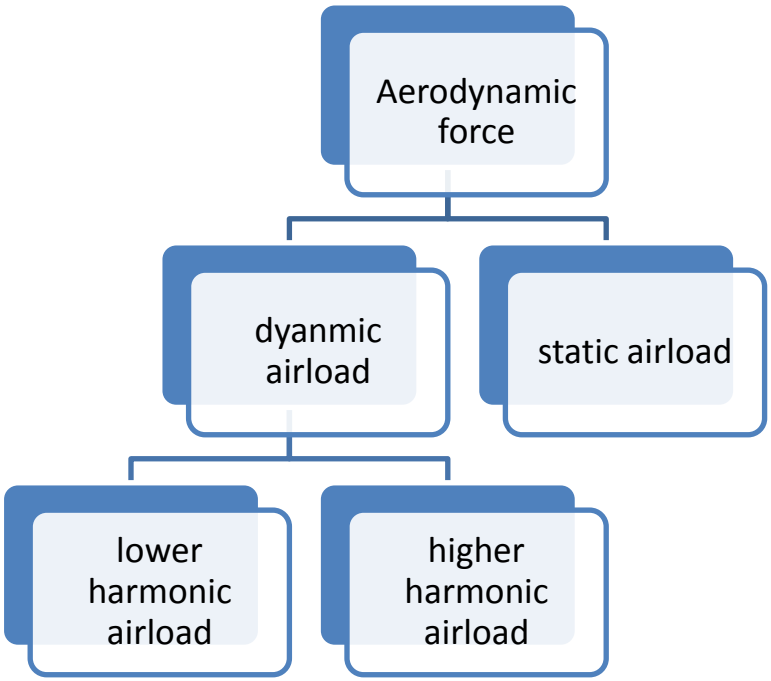

Figure 36: Aerodynamic force category

5.3.2 Further Parametric Study in Time Domain

The hub load in time domain has almost the same characteristics as the hub load in frequency domain. Figure 37 shows the hub load in one period of two MEMP beam with different spring stiffness for 4th harmonic aerodynamic force.

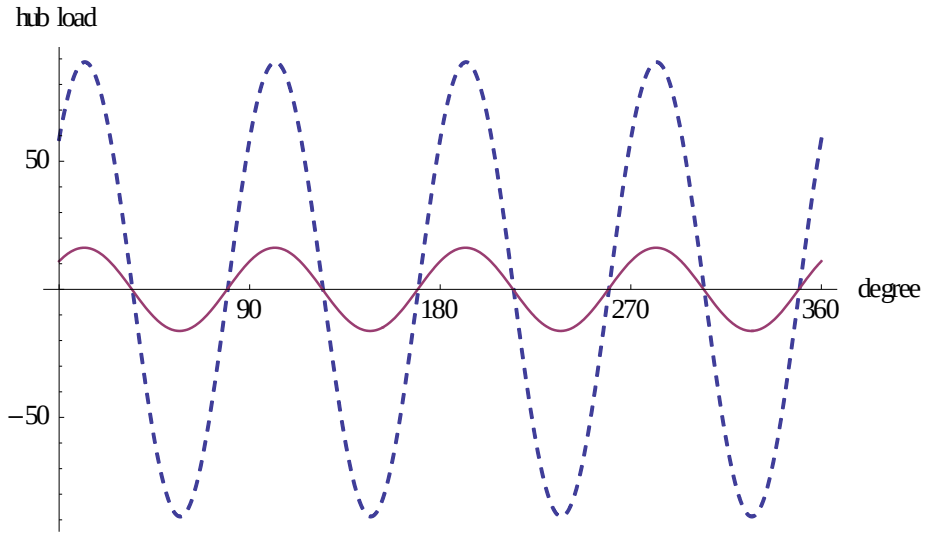

Figure 37: Hub load time history. X axis: azimuthal angle in degrees. Y axis: nondimensional hub load. Dashed curve: MEMP beam with strong springs for connection. Smooth curve: MEMP beam with soft springs for connection.

The result confirms the conclusion made before that a soft spring between the shell and spar makes a better vibration reduction.

For the same harmonic, Figure 35 illustrates two hub loads of MEMP beams with different boundary springs.

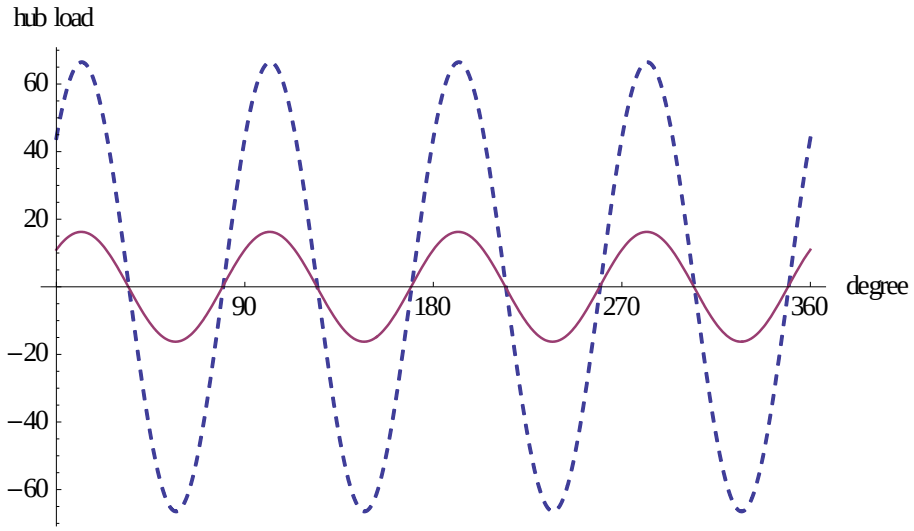

Figure 38: Hub load time history. X axis: azimuthal angle in degrees. Y axis: nondimensional hub load. Dashed curve: MEMP beam with strong boundary springs for the shell. Smooth curve: MEMP beam with soft boundary springs for the shell.

Again, the result is consistent with the conclusion made before that a soft boundary spring of the shell makes a better vibration reduction. Many simulations have been conducted to verify the consistency between the hub load functions in frequency domain and in time domain. However, there are other cases that show the difference between them. Figure 39 gives one possible configuration of MEMP design that actually amplifies the vibration for the 3rd harmonic aerodynamic force.

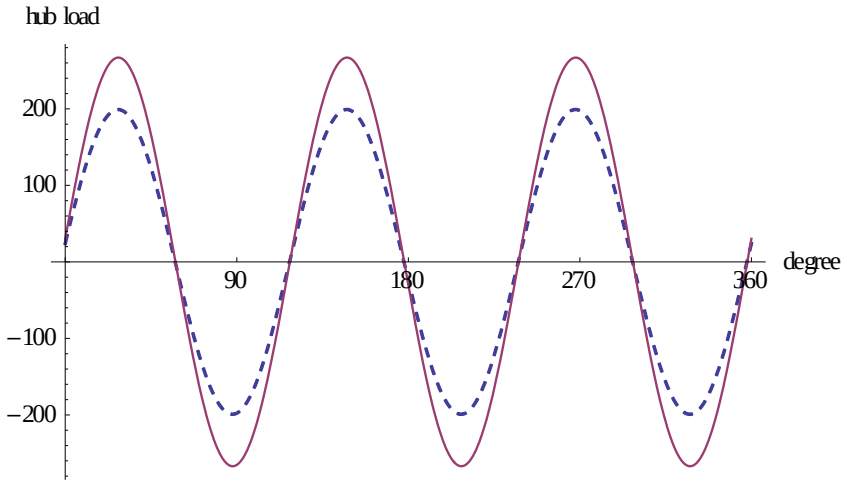

Figure 39: Hub load time history. X axis: azimuthal angle in degrees. Y axis: nondimensional hub load. Dashed curve: MEMP beam with small springs (S_c =10). Smooth curve: MEMP beam with strong springs (S_c =100).

This figure shows the opposite result compared with previous simulations. The strong springs actually produce more vibration reduction. Such behavior can be well explained in next two figures.

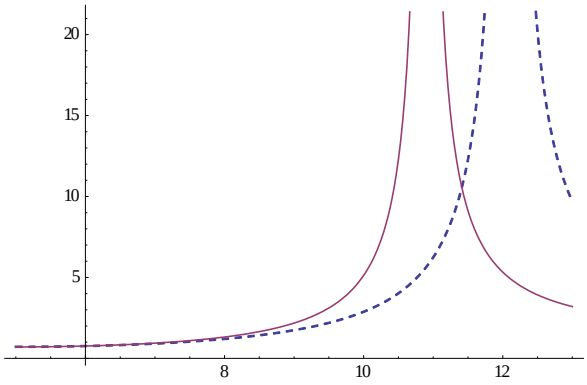

Figure 40: Hub load transfer function in frequency domain for cosine component of third harmonic aerodynamic force. X axis: $\left(\frac{\omega}{\Omega}\right)^2$. Y axis: hub load

transfer function. Dashed curve: MEMP beam with strong springs (S_c =100). Smooth curve: MEMP beam with small springs (S_c =10).

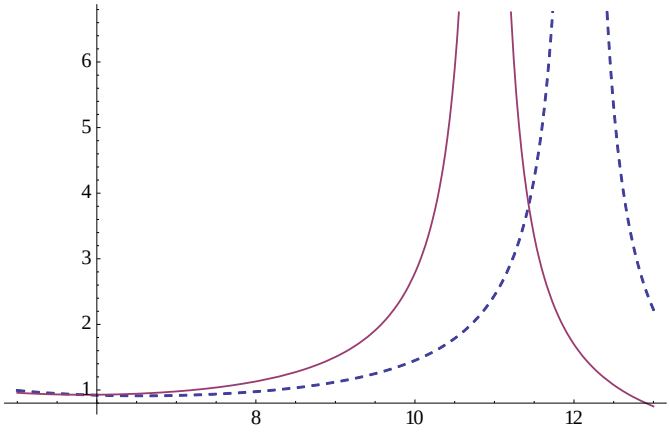

Figure 41: Hub load transfer function in frequency domain for sine component of third harmonic aerodynamic force. X axis: $\left(\frac{\omega}{\Omega}\right)^2$. Y axis: hub load transfer function. Dashed curve: MEMP beam with strong springs (S_c =100). Smooth curve: MEMP beam with small springs (S_c =10).

Both figures give the hub load transfer function for the third harmonic of aerodynamic force, in which $\left(\frac{\omega}{\Omega}\right)^2 = 9$. As can be seen, although the smooth curve has small spring stiffness, it is higher than the dashed curve at $\left(\frac{\omega}{\Omega}\right)^2 = 9$, which is the case with strong spring stiffness. The reason is that the small spring stiffness shifts the peak towards left in frequency domain, which makes it closer to $\left(\frac{\omega}{\Omega}\right)^2 = 9$ and thus significantly increases the value of transfer function. Although the overall hub load transfer function for small spring stiffness is smaller than that for strong spring stiffness,

it is not the case at this local frequency. This phenomenon complicates the study of hub load in time domain because it is difficult to prevent the unwanted situation from happening for all harmonics. In single beam model, this is also a big concern. Many simulations have been done to investigate this issue and it turns out the third, fourth and fifth harmonics are the ones that matter the most as the force amplitudes for these three harmonics are the largest. In order to obtain a better vibration reduction, these three harmonics should be considered first. One of the solutions to this issue is to change the parameters to move peaks away from those frequencies ($\omega = n\Omega$). It is advantageous that the MEMP structure, which involves more parameter choices, provides more opportunities to tune the design to avoid vibration peaks. In section 5.2, it has been revealed that the torsional spring, the bending stiffness and the difference in beam properties are able to alter the structure's natural frequencies. Therefore, they are of great use in improving the MEMP structure's performance in time domain.

5.3.3 Comparison between Two Designs in Time Domain

This section presents the hub load in time domain for both single beam and MEMP designs and demonstrates that MEMP design has a critical advantage in vibration reduction.

Figure 42 shows a comparison of hub loads in time domain between these two designs, in which the aerodynamic force is described by harmonics from three to ten. The parameters in MEMP design are determined by a number of simulations for a better performance. It can be seen that the MEMP beam reduces substantial vibration.

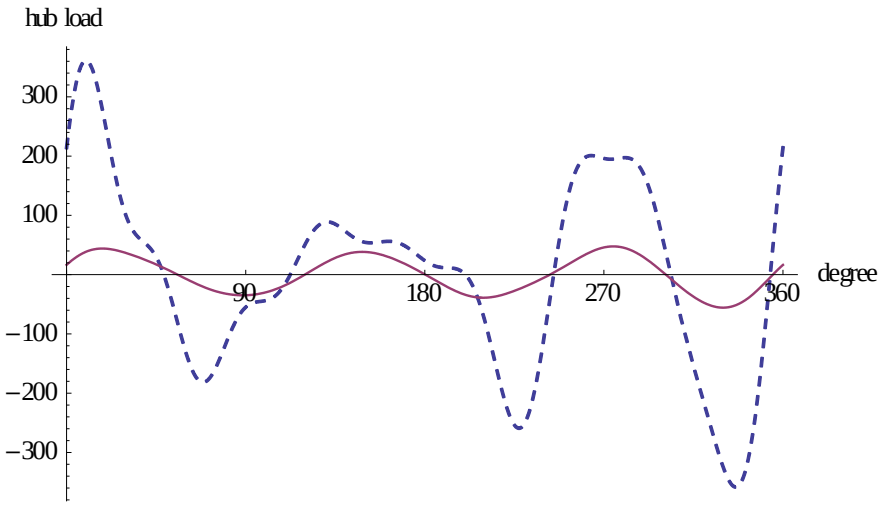

Figure 42: Hub load comparison between MEMP beam and single beam in one full period. X axis: azimuthal angle in degrees. Y axis: nondimensional hub load. Dashed curve: single beam. Smooth curve: MEMP beam.

To quantify the vibration reduction, the mean square hub load has been calculated.

The mean square hub load of MEMP beam: 921.77

The mean square hub load of single beam: 25491.40

The vibration reduction in dB: 7.2dB

This result looks good in terms of the huge vibration reduction. However, there is a problem with it, which will be discussed in the next section.

5.5 Blade Deflection

5.5.1 Introduction

To be consistent with the aerodynamic force, the blade deflection falls into two categories: the static deflection and the dynamic deflection. The dynamic deflection can be further divided into the lower harmonic deflection and the higher harmonic deflection. The static deflection is caused by the static airload, the 0^{th} harmonic of the aerodynamic force, which is the lift that holds the helicopter. Like the static airload, the static deflection is only spatial dependent. The lower harmonic deflection is the deflection caused by the lower harmonic airload, the first and second harmonics of aerodynamic force. The higher harmonic deflection is due to the higher harmonic airload, the aerodynamic force harmonics from three to ten. Both lower harmonic deflection and higher harmonic deflection is time and spatial dependent. The average deflection is the mean value of the deflections of spar and shell. To maintain an enough static strength, MEMP blade's average deflection at tip should not be much larger than that of a traditional blade. The relative deflection is defined as the deflection difference between the shell and the spar. To prevent the shell and spar from collision, the space between them must be larger than the relative deflection. The following diagram displays the relations for different deflections.

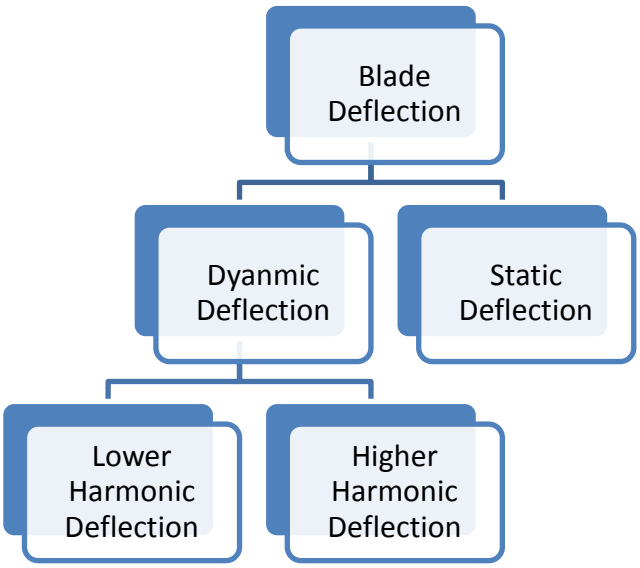

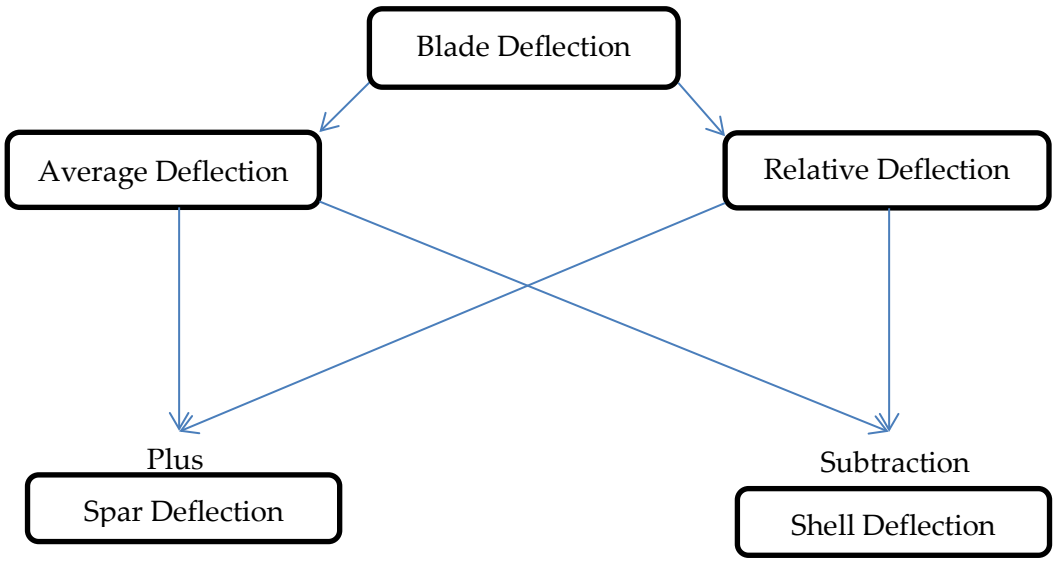

Figure 43: Deflection category

5.5.1 Problem Statement and Solutions

Despite the excellent vibration reduction performance for MEMP design, the associated deflection has become a critical concern for this new concept. This section deals with two major deflection problems emerging from this work.

(1) Average Static Deflection

In MEMP design, the blade is divided into two parts: the spar and the shell, which are characterized as two beams. To conserve the mass, two thinner beams are less stiff than a single thick beam. This fact results in a reduced static strength for the MEMP blade compared with the traditional blade. As stated previously, the torsional springs between the shell and spar are introduced to solve such issue. The average static deflection at the tip is a critical quantity reflecting the static strength. Figure 44 shows how it changes in traditional and MEMP designs under the realistic airload at certain time.

As can be seen, the MEMP beam model without torsional spring has a larger tip deflection compared with single beam model. After applying the torsional spring, the tip deflection is reduced to a point smaller than the single beam model, which suggests the torsional springs is an effective method to maintain enough static strength.

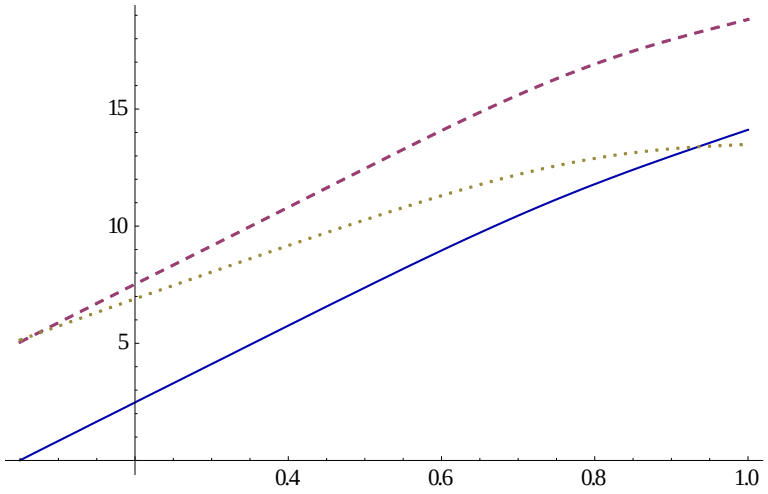

Figure 44: Average static deflection with conserved mass. X axis: radial position. Y axis: deflection in inches. Smooth curve: single beam model deflection. Dashed curve: MEMP beam model deflection with no torsional springs. Dotted curve: MEMP beam model deflection with torsional springs.

(2) Relative Deflection

To prevent the shell and spar from collision, the space between them must be larger than the relative deflection. For a helicopter, the blade thickness is less than 2 inches. However, the relative deflection between two beams in MEMP design can be as large as several feet in some cases studied, which has no practical use. Therefore, an approach to diminish the relative deflection while maintaining the vibration reduction performance has become an important goal. Figure 45 and Figure 46 illustrate the relative deflection of the MEMP blade shown in Figure 42.

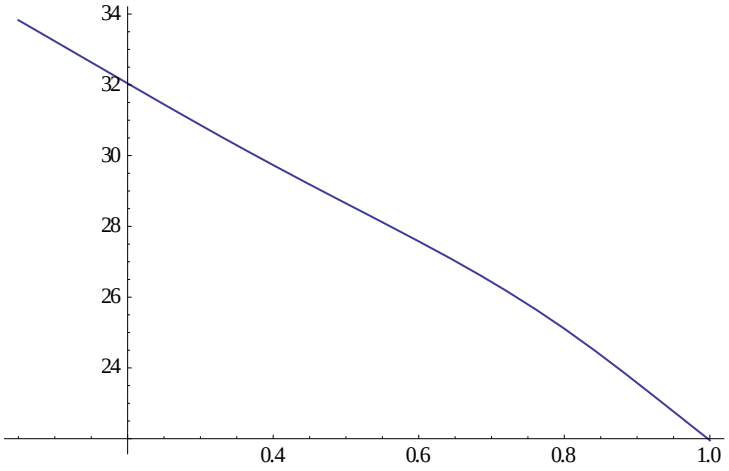

Figure 45: Relative static deflection along a MEMP blade. X axis: radial position. Y axis: deflection in inches

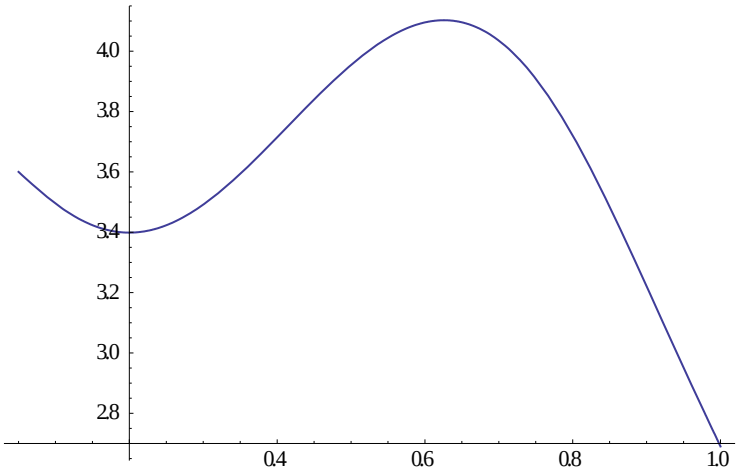

Figure 46: Relative dynamic deflection along a MEMP blade at certain azimuthal angle. X axis: radial position. Y axis: deflection in inches

In order to obtain a significant vibration reduction, the boundary linear spring of the shell is small and the springs between the shell and spar are triangular distributed. Therefore, the maximum relative static deflection, which is up to 34 inches, occurs at the root. Clearly, it is too much for a helicopter blade. For the relative dynamic deflection,

the maximum value exceeds 4 inches, which is also too much for a helicopter blade. Many simulations have been done to explore the approaches to diminish the relative deflection and several methods have been found. They are listed below:

1. Increase the number of blades
2. Pre-compress springs between the shell and spar
3. Increase stiffness of the springs between the shell and the spar and the boundary spring
4. Distribute proper non-uniform springs
5. Weight the shell
6. Add damping into system
7. Employ nonlinear spring.

The first solution decreases the aerodynamic force on each rotor blade, thus diminishes the deflection. The second method decreases the relative static deflection. The third is easy to apply but the penalty is apparent - the worse vibration reduction. Distributing the spring in a certain way is effective on reducing the relative deflection but requires more expense on manufacturing. Weighting the shell is effective and currently under investigation. Adding damping into the system results in a significant deflection reduction but also sacrifices the vibration reduction performance. The last approach has the minimum cost but needs more investigation.

5.2 Relative Dynamic Deflection Control

Although the relative static deflection is much larger than the relative dynamic deflection, the static one is easier to control than the dynamic one, as the static deflection is only spatial dependent. The dynamic deflection, however, is the outcome of the dynamic characteristics of the whole system controlled by more than ten parameters, thus more complicated to control. In order to simplify the analysis process for relative dynamic deflection, only the maximum relative deflection is investigated. The goal of relative dynamic deflection control is to minimize the maximum relative deflection.

(1) Spring stiffness

Increasing the spring stiffness is the most apparent way to control deflection. Table 3 indicates that spring stiffness has a considerable influence on maximum relative dynamic deflection. Boundary spring has the same effect on maximum relative dynamic deflection. However, as demonstrated before, the strong spring stiffness significantly weaken the MEMP design's capacity to reduce the vibration. Many experiments have been done to explore the most effective way to set up springs and it turns out a triangular spring distribution will achieve a balance between the deflection and vibration reduction. The boundary spring also should be set in a way such that the maximum relative dynamic deflection occurs both at the root and somewhere along the

beam. If the maximum deflection only occurs at root, it means the boundary spring is too weak or the spring between shell and spar is too strong.

Table 3: Maximum relative deflection

	Spring stiffness parameter S_c	maximum relative dynamic deflections (inches)
Case 1	10	2
Case 2	4	10
Case 3	1	12

(2) Weight the shell

As demonstrated in previous section, the MEMP design with different weight of shell and spar has little effect on hub load transfer function except changing the natural frequencies. But it does influence the deflection. Some experiments have been done and they reveal that a heavier shell is able to reduce the deflection. The reason is somewhat apparent because a heavier shell has more inertia so its deflection reduces.

(3) Adding damping

This turns out to be a very effective way to diminish the deflection although it puts penalty on vibration reduction. Table 4 illustrates this phenomenon.

Table 4: Damping effect

	Spring stiffness parameter S_c	maximum relative dynamic deflection (inches)	Vibration reduction in dB
MEMP design with damping	$1.5x(1+0.5\omega i)$	6	4.4
MEMP design without damping	$1.5x$	7	4.7

(4) Nonlinear spring structure

Further investigation on relative dynamic deflection reveals that the relative deflection due to first two harmonics (relative lower harmonic deflection) is much larger than the deflection caused by harmonics from 3rd to 10th (relative higher harmonic deflection). Table 5 lists the total maximum relative dynamic deflection and the maximum relative higher harmonic deflection for the two cases displayed in table 4. As can be seen, the relative higher harmonic deflection is only a small part of total relative dynamic deflection. The main contribution of relative dynamic deflection is from lower

harmonics. Also, we can see the added damping mainly affects the relative dynamic deflection due to the higher harmonics but have little impact on the first two harmonics' deflection.

Table 5: Maximum relative dynamic and higher harmonic deflections

	maximum relative dynamic deflection (inches)	maximum relative higher harmonic deflection (inches)
MEMP design with damping	6	1.5
MEMP design without damping	7	2

With this fact, the nonlinear spring can be of great use. The nonlinear spring is the kind of spring that has different stiffness. Figure 47 gives an example.

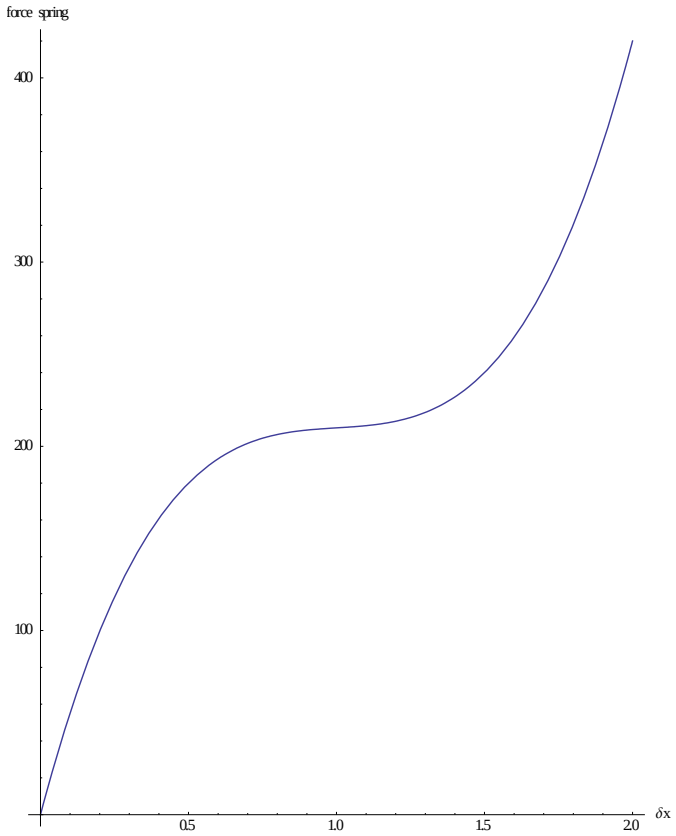

Figure 47: Nonlinear spring. X axis: displacement. Y axis: spring force

The spring shown in the figure is strong at two ends and soft in the middle. If the MEMP beam equilibrium position happens to be inside the region with small stiffness, the vibration will be governed by the small spring stiffness, which guarantees enough vibration reduction. Only the lower harmonics, which generates more deflection, will push the shell out of the region with small stiffness. But the strong stiffness at two ends will significantly resist such movement, thus preventing the deflection from growing too much.

For example, if a soft distributed spring ($S_c(x) = x$) is maintained in the middle of the nonlinear spring displacement, the vibration reduction shown in Figure 42 can be achieved. The relative higher harmonic deflection is up to 2 inches, see Figure 48.

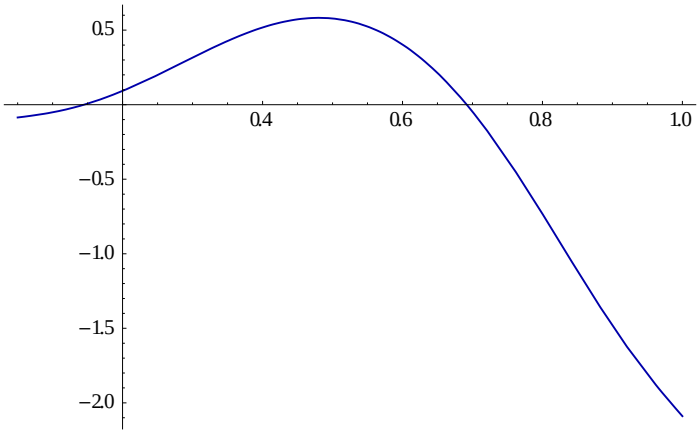

Figure 48: Relative higher harmonic deflection for $S_c(x) = x$

If a strong distributed spring ($S_c(x) = 60x$) exists at two ends of the nonlinear spring displacement, the relative lower harmonic deflection is around 2 inches, see Figure 49.

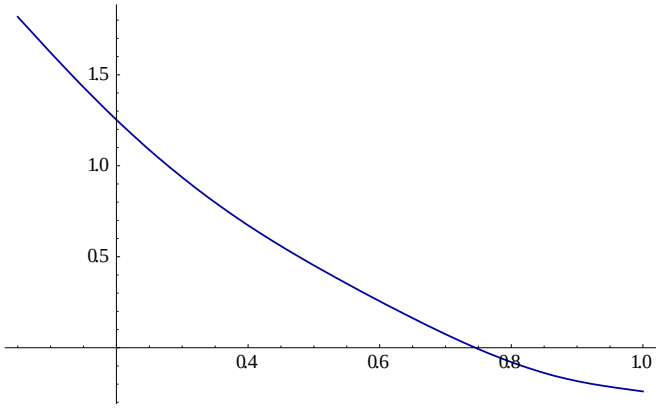

Figure 49: Relative lower harmonic deflection for $S_c(x) = 60x$

In the worst case, the total relative dynamic deflection would be 4 inches (2+2=4). If the strong spring ($S_c(x) = 60x$) is also used to support the helicopter weight, the zeroth airload harmonic, the maximum relative static deflection is around 4 inches occurring the root, see Figure 50.

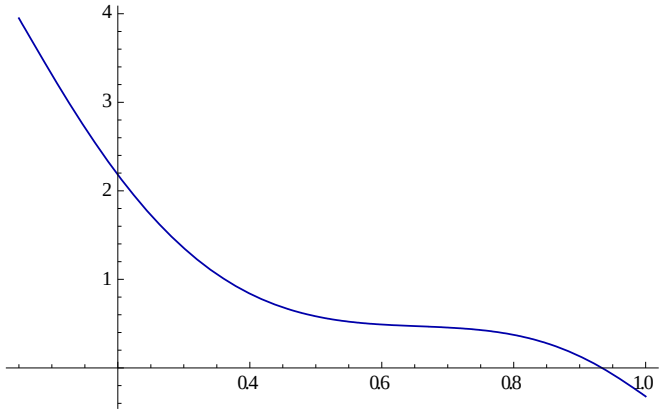

Figure 50: Relative static deflection for $S_c(x) = 60x$

Thus, a structure shown below can ensure both a good vibration reduction and a blade thickness of 8 inches.

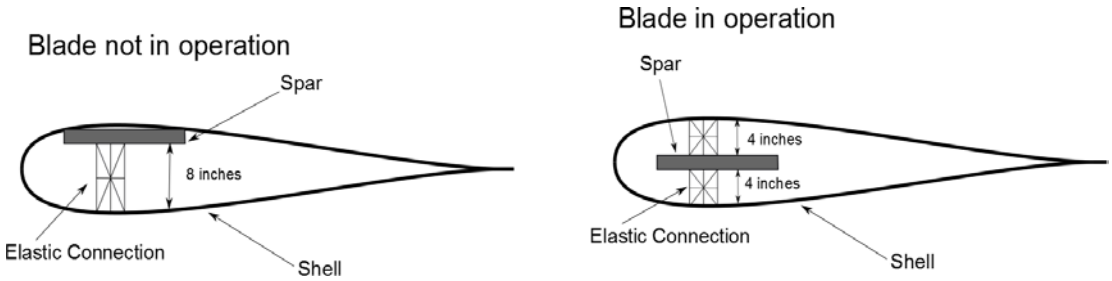

Figure 51: MEMP blade with nonlinear spring

When blade is not in operation, the spar is located at the top of shell to leave enough space below. When in operation, the static airload pushes the shell upward to

make the spar stay in the middle, leaving both upper and lower space of 4 inches for vibration. This kind of structure has a total thickness of 8 inches. Although the thickness in this example is still too much for a helicopter blade, it can be reduced by adjusting the critical parameters or further employing the methods discussed above.

It needs to be emphasized that the analysis made above is just a rough estimation. But it provides a general idea regarding how a nonlinear spring suspension helps in designing the MEMP blade to meet the vibration reduction. More accurate theoretical analysis, such as nonlinear theory and energy balance, will be needed in the future.

5.5.3 Nonlinear Spring Structure

This section proposes two nonlinear spring models.

(1) Slider mechanism

Figure 46 shows the slider mechanism. It consists of two tracks, two sliders, a solid bar connecting slider A and B and a spring attached between the wall and slider B.

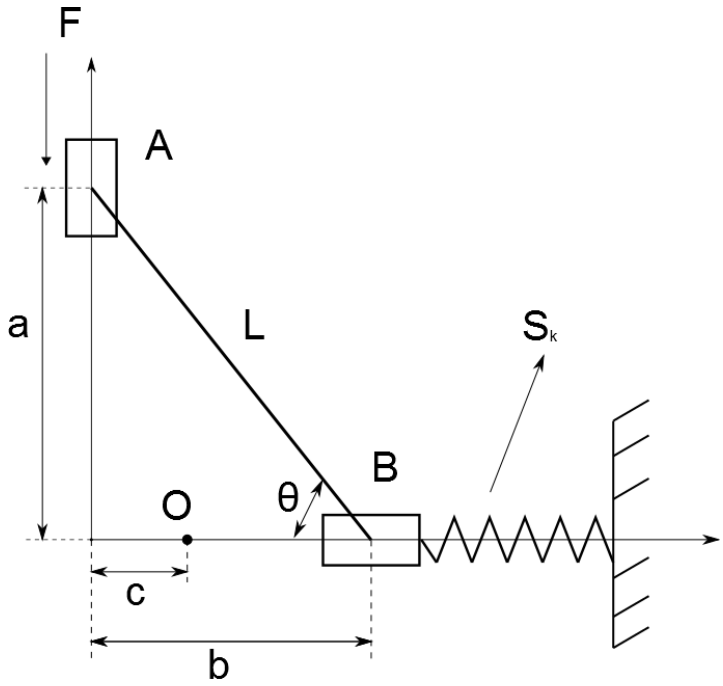

Figure 52: Slider mechanism

In operation, the slider A is pushed by external force F. To maintain the force balance,

$$F = F_s \tan\theta, \text{ where } F_s - \text{spring force}$$

Assume that the free position of spring locates at O and the length of solid bar to be l, so $F_s = S_k(b-c)$, then,

$$F = S_k(b-c)\tan\theta = S_k(b\tan\theta - c\tan\theta)$$
$$= S_k(a - \frac{ac}{\sqrt{l^2-a^2}}) = S_k(1 - \frac{c}{\sqrt{l^2-a^2}})a$$

If d is the displacement driven by force F, then,

$$F = S_k(1 - \frac{c}{\sqrt{l^2 - (1-d)^2}})(1-d)$$

Figure 43 gives the plot of spring force versus displacement.

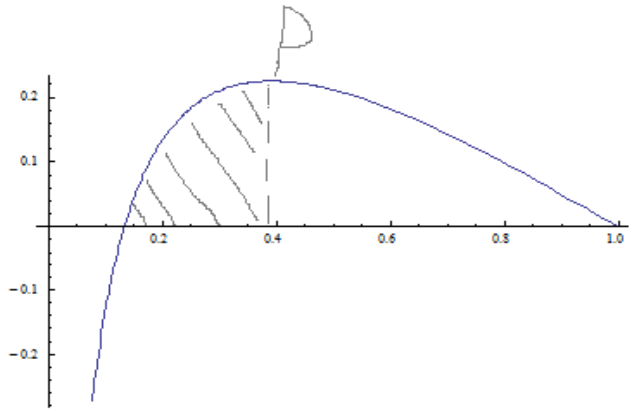

Figure 53: Spring force VS displacement. X axis: displacement. Y axis: spring force

The shaded part in Figure 47 forms the left part of Figure 45, which means the slider mechanism is able to function like part of a nonlinear spring. The right half of Figure 41 can readily be achieved by adding another spring that begins to resist the movement of slider A after it passes point P.

(2) Piston mechanism

Figure 48 illustrates this design. It consists of a vessel and a piston. The vessel's cross section becomes smaller and smaller with different rate from A to C. If the pressure in the vessel is assumed unchanged and the piston moves from A to C, the

force that holds the piston will become weaker and weaker with different rate. The force VS displacement plot looks like the left half of Figure 45.

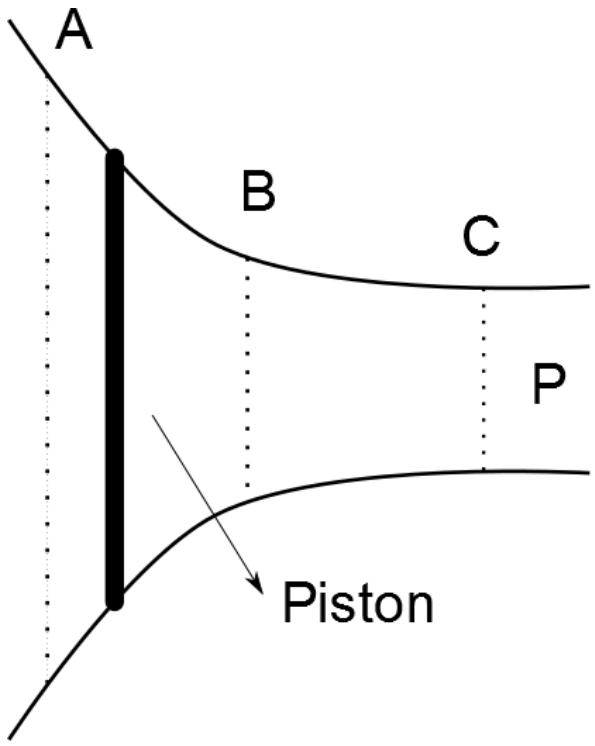

Figure 54: Piston mechanism

However, this design requires a piston that can change its area continuously, which is difficult to design and manufacture, and the condition that the pressure is unchanged when piston goes from A to C is hard to implement.

6. Conclusion and Future Work

6.1 Conclusion

The possibility of applying MEMP design to helicopter rotor blade is studied in this thesis, which involves model development, numerical simulation and parametric study. A number of realistic parameters are used for the purpose of assessing whether this idea is feasible. The result shows the MEMP design has a huge capacity to reduce the hub vibration. The spring between the shell and spar, and the one at the boundary play a critical role in such vibration reduction. The bending stiffness and the mass of the shell and spar also affect such vibration reduction by altering the natural frequencies of the structure. Without much penalty on vibration reduction, the required static strength for this structure is reinforced by a torsional spring between the shell and spar. In addition, some other factors including the distribution of mass, bending stiffness and spring stiffness have considerable effects on the MEMP design performance. By choosing proper parameters, the hub load in frequency domain can be significantly reduced. In time domain, the vibration reduction is further influenced by the harmonics of realistic aerodynamic force. A desirable performance can be achieved if all harmonics avoid structural resonances.

Despite a huge advantage in vibration reduction, the large relative deflection of the MEMP design needs to be diminished before its application to helicopter rotor. The

unwanted deflection is primarily due to the large static load and the big variation in aerodynamic force. Several methods to deal with this issue are proposed in this thesis. Two of them, the parametric study and the nonlinear spring, are discussed in detail. However, more future work is required to solve this issue completely.

6.2 Future Work

In order to obtain a desirable performance of vibration reduction and maintain an acceptable deflection for the MEMP blade design, more work needs to be done in the future.

The priority is to attain a thorough understanding on each nondimensional parameter. Until now, only a general knowledge on these nondimensional parameters has been revealed. However, the effects of some parameters are still unclear, such as the spatial distribution of spring stiffness, mass and bending stiffness.

Second, the idea of nonlinear spring needs to be further developed in terms of its effects on deflection reduction and structure design. Nonlinear theory is required to analyze the interaction of nonlinear spring and the beams. If a mathematical description of such nonlinear spring can be obtained, more work can be done on the design process.

Another topic for future research is the need to develop a general multi-variable search algorithm that finds optimum solutions for vibration reduction subject to

constraints. The present study has shown that it is difficult to identify robust optimum solutions manually in a system with so many parameters. An algorithm of this type would be a valuable contribution to the field of MEMP design for any system. MEMP is always going to have many more adjustable parameters than traditional designs, and there needs to be an approach to find optimum solutions subject to constraints (weight, static strength, etc.). The complexity of such a system is both a disadvantage and an advantage. While such systems are harder to analyze and understand, the large number of parameter choices also provides more ways to tune the system to achieve goals, and of course the potential for vibration reduction is very great.

Finally, further improvement for the MEMP blade and the application of MEMP design for other types of rotors, such as wind turbine and gas compressors, will be studied in the future.

Appendix A

The first harmonics of CH 34 blade aerodynamic force
X axis: radial position. Y axis: airload (lb/in)

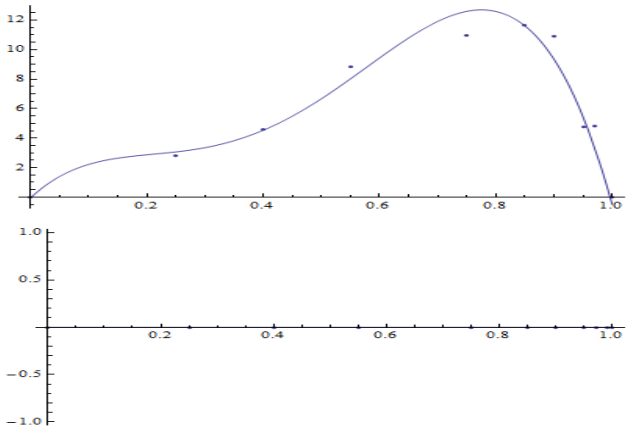

The second harmonic of CH 34 blade aerodynamic force
X axis: radial position. Y axis: airload (lb/in)

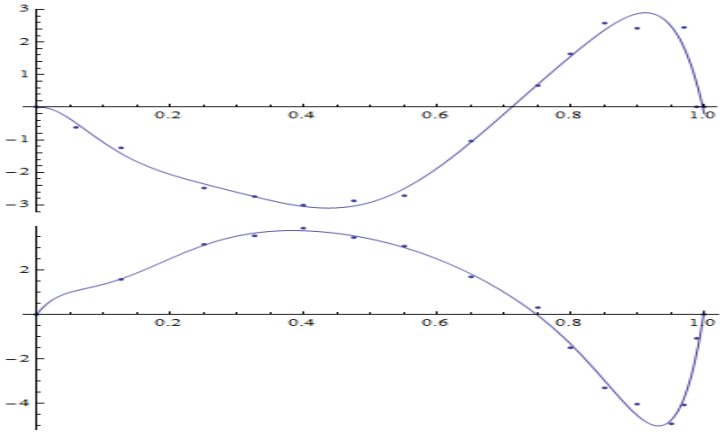

The third harmonic of CH 34 blade aerodynamic force
X axis: radial position. Y axis: airload (lb/in)

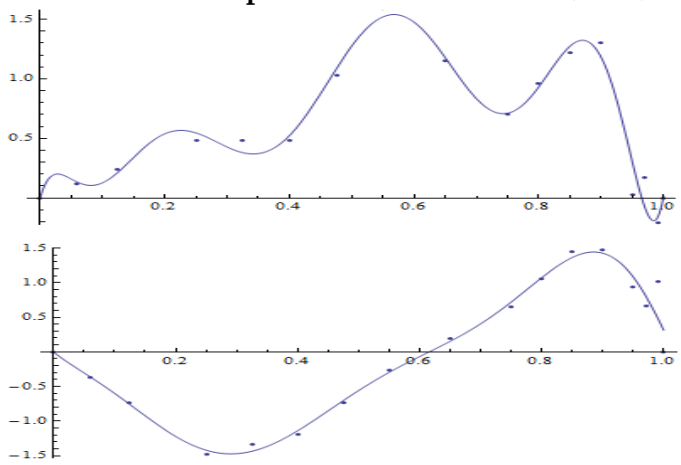

The fourth harmonic of CH 34 blade aerodynamic force
X axis: radial position. Y axis: airload (lb/in)

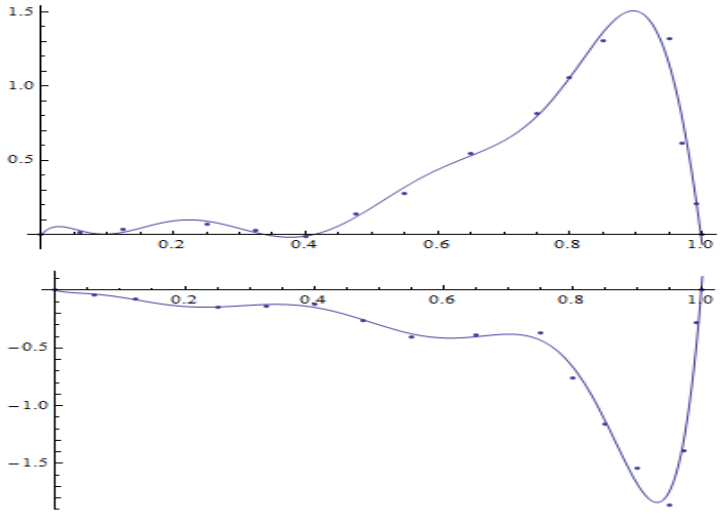

The fifth harmonic of CH 34 blade aerodynamic force
X axis: radial position. Y axis: airload (lb/in)

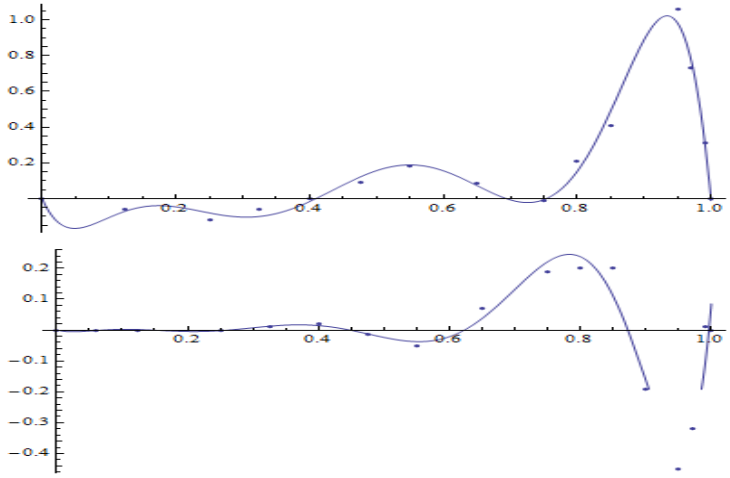

The sixth harmonic of CH 34 blade aerodynamic force
X axis: radial position. Y axis: airload (lb/in)

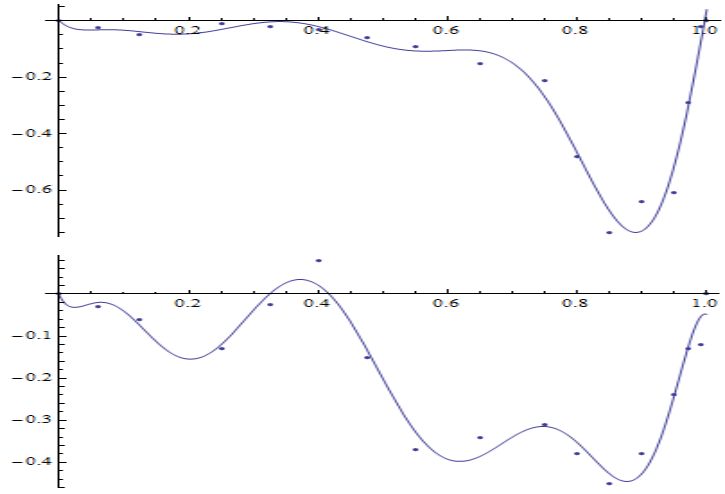

The seventh harmonic of CH 34 blade aerodynamic force
X axis: radial position. Y axis: airload (lb/in)

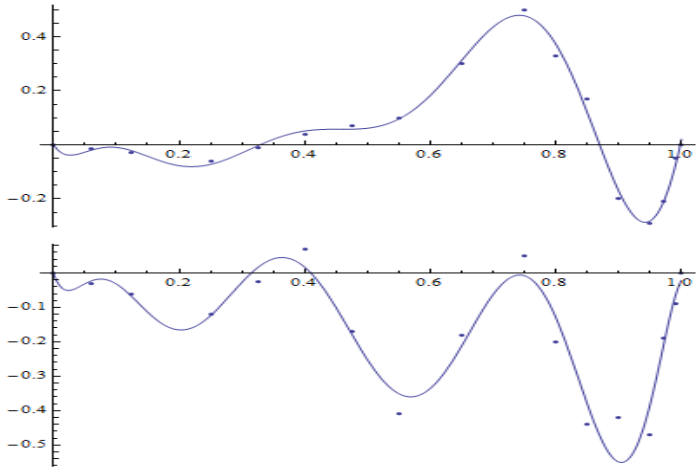

The eight harmonic of CH 34 blade aerodynamic force
X axis: radial position. Y axis: airload (lb/in)

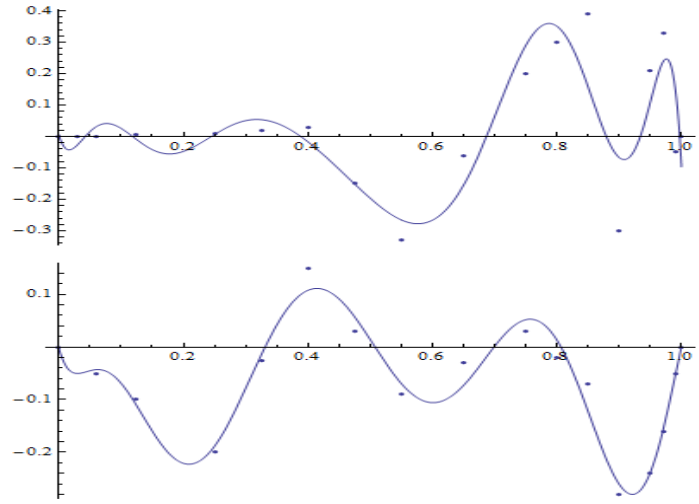

The ninth harmonic of CH 34 blade aerodynamic force
X axis: radial position. Y axis: airload (lb/in)

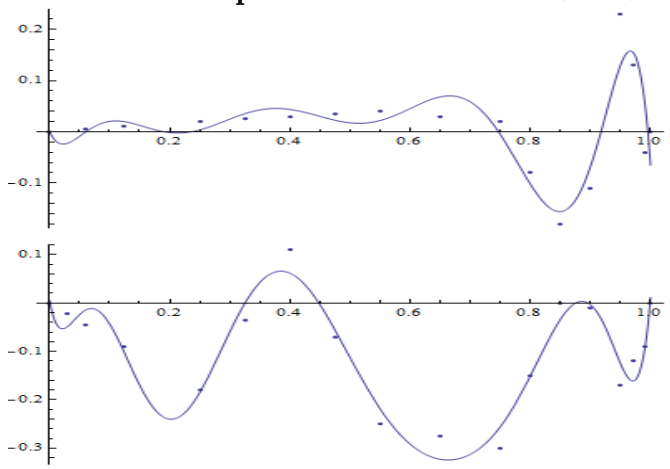

The tenth harmonic of CH 34 blade aerodynamic force
X axis: radial position. Y axis: airload (lb/in)

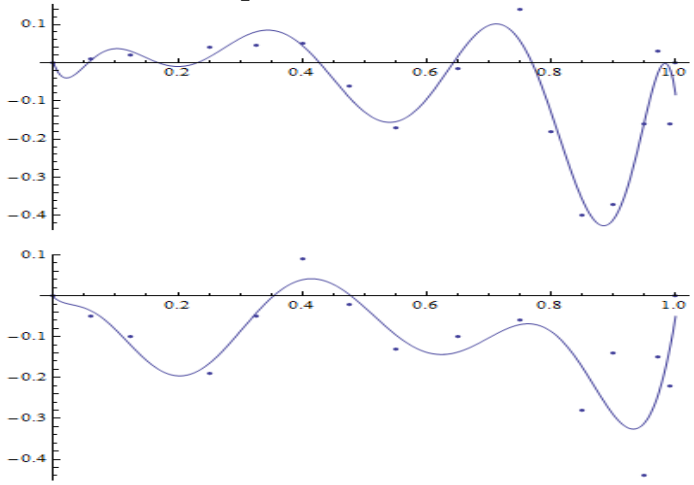

Appendix B

Wolfram Mathematical program for solving deflection and hub load:

```
Clear[A,B,ϕ]
A[n_]:=Array[a,n,0]
B[n_]:=Array[b,n,0]
ϕ[n_,x_]:=Array[x^#&,n,0]
equ1[n_,k1_,λ1_,μ1_,ν1_,β_,x_]:=(2β*ϕ[n,x]-2λ1*D[D[D[D[ϕ[n,x],x],x],x],x]+(1-
x^2+2μ1+2ν1)D[D[ϕ[n,x],x],x]-2x*D[ϕ[n,x],x]-2k1*ϕ[n,x]).A[n]+2(k1*ϕ[n,x]-μ1
D[D[ϕ[n,x],x],x]+ν1 D[D[ϕ[n,x],x],x]).B[n]
equ2[n_,k2_,λ2_,μ2_,ν2_,β_,p_,x_]:=(2β*ϕ[n,x]-2λ2*D[D[D[D[ϕ[n,x],x],x],x],x]+(1-
x^2+2μ2+2ν2)D[D[ϕ[n,x],x],x]-2x*D[ϕ[n,x],x]-2k2*ϕ[n,x]).B[n]+2(k2*ϕ[n,x]-μ2
D[D[ϕ[n,x],x],x]+ν2 D[D[ϕ[n,x],x],x]).A[n]+2p
trun1[n_,k1_,λ1_,μ1_,ν1_,β_]:=Take[CoefficientList[equ1[n,k1,λ1,μ1,ν1,β,x],x],n-4]
trun2[n_,k2_,λ2_,μ2_,ν2_,β_,p_]:=Take[CoefficientList[equ2[n,k2,λ2,μ2,ν2,β,p,x],x],n
-4]
trun[n_,k1_,k2_,λ1_,λ2_,μ1_,μ2_,ν1_,ν2_,β_,p_]:=Join[trun1[n,k1,λ1,μ1,ν1,β],trun2[n
,k2,λ2,μ2,ν2,β,p]]
equmat[n_,k1_,k2_,λ1_,λ2_,μ1_,μ2_,ν1_,ν2_,β_,p_]:=CoefficientArrays[trun[n,k1,k2,λ
1,λ2,μ1,μ2,ν1,ν2,β,p],Join[Array[a,n,0],Array[b,n,0]]]
bcmat[n_,
λ1_,λ2_,μ1_,μ2_,ν1_,ν2_,β_,f_,κh1_,κa1_,κh2_,κa2_]:=CoefficientArrays[{(A[n].D[
D[ϕ[n,l],l],l]/.l→1)==0,(μ1 A[n]. D[ϕ[n,l],l]/.l→1)-(μ1 B[n]. D[ϕ[n,l],l]/.l→1)+(ν1 A[n].
D[ϕ[n,l],l]/.l→1)+(ν2 B[n]. D[ϕ[n,l],l]/.l→1)-(λ1
A[n].D[D[D[ϕ[n,l],l],l],l]/.l→1)==0,(B[n].D[D[ϕ[n,l],l],l]/.l→1)==0,(μ2 B[n].
D[ϕ[n,l],l]/.l→1)-(μ2 A[n]. D[ϕ[n,l],l]/.l→1)+(ν1 B[n]. D[ϕ[n,l],l]/.l→1)+(ν2 A[n].
D[ϕ[n,l],l]/.l→1)-(λ2 B[n].D[D[D[ϕ[n,l],l],l],l]/.l→1)==f,-
λ1(A[n].D[D[D[ϕ[n,l],l],l],l]/.l→0.05) +(0.9975/2 +μ1+ν1)(A[n].D[ϕ[n,l],l]/.l→0.05)-
μ1(B[n].D[ϕ[n,l],l]/.l→0.05)+ν1(B[n].D[ϕ[n,l],l]/.l→0.05)-κh1
(A[n].ϕ[n,l]/.l→0.05)==0,λ1 (A[n].D[D[ϕ[n,l],l],l]/.l→0.05)-κa1
(A[n].D[ϕ[n,l],l]/.l→0.05)==0,-λ2 (B[n].D[D[D[ϕ[n,l],l],l],l]/.l→0.05)+(0.9975/2
+μ2+ν2)(B[n].D[ϕ[n,l],l]/.l→0.05)-
μ2(A[n].D[ϕ[n,l],l]/.l→0.05)+ν2(A[n].D[ϕ[n,l],l]/.l→0.05)-κh2
(B[n].ϕ[n,l]/.l→0.05)==0,λ2(B[n].D[D[ϕ[n,l],l],l]/.l→0.05)-κa2
(B[n].D[ϕ[n,l],l]/.l→0.05)==0},Join[Array[a,n,0],Array[b,n,0]]]
coeffmat[n_,k1_,
k2_,λ1_,λ2_,μ1_,μ2_,ν1_,ν2_,β_,p_,f_,κh1_,κa1_,κh2_,κa2_]:=Join[equmat[n,k1,k2,λ
1,λ2,μ1,μ2,ν1,ν2,β,p][[2]],bcmat[n,λ1,λ2,μ1,μ2,ν1,ν2,β,f,κh1,κa1,κh2,κa2][[2]]]
```

```
forcvec[n_,k1_, k2_,λ1_,λ2_,μ1_,μ2_,ν1_,ν2_,β_,p_,f_,κh1_,κa1_,κh2_,κa2_]:=Join[-
equmat[n,k1,k2,λ1,λ2,μ1,μ2,ν1,ν2,β,p][[1]],-
bcmat[n,λ1,λ2,μ1,μ2,ν1,ν2,β,f,κh1,κa1,κh2,κa2][[1]]]
solnvec[n_,k1_,
k2_,λ1_,λ2_,μ1_,μ2_,ν1_,ν2_,β_,p_,f_,κh1_,κa1_,κh2_,κa2_]:=LinearSolve[coeffmat[
n,k1, k2,λ1,λ2,μ1,μ2,ν1,ν2,β,p,f,κh1,κa1,κh2,κa2],forcvec[n,k1,
k2,λ1,λ2,μ1,μ2,ν1,ν2,β,p,f,κh1,κa1,κh2,κa2]]
h1[n_,k1_,
k2_,λ1_,λ2_,μ1_,μ2_,ν1_,ν2_,β_,p_,f_,κh1_,κa1_,κh2_,κa2_,x_]:=Take[solnvec[n,k1,
k2,λ1,λ2,μ1,μ2,ν1,ν2,β,p,f,κh1,κa1,κh2,κa2],n].Array[x^#&,n,0]
h2[n_,k1_,
k2_,λ1_,λ2_,μ1_,μ2_,ν1_,ν2_,β_,p_,f_,κh1_,κa1_,κh2_,κa2_,x_]:=Take[solnvec[n,k1,
k2,λ1,λ2,μ1,μ2,ν1,ν2,β,p,f,κh1,κa1,κh2,κa2],-n].Array[x^#&,n,0]
tranfun[n_,k1_,
k2_,λ1_,λ2_,μ1_,μ2_,ν1_,ν2_,β_,p_,f_,κh1_,κa1_,κh2_,κa2_]:=Abs[1/(Integrate[p,{x,
0.05,1}]+f)*{(k2 κh1)/k1 ,κh2}.{h1[n,k1,
k2,λ1,λ2,μ1,μ2,ν1,ν2,β,p,f,κh1,κa1,κh2,κa2,0.05],h2[n,k1,
k2,λ1,λ2,μ1,μ2,ν1,ν2,β,p,f,κh1,κa1,κh2,κa2,0.05]}]
forcefun[n_,k1_,
k2_,λ1_,λ2_,μ1_,μ2_,ν1_,ν2_,β_,p_,f_,κh1_,κa1_,κh2_,κa2_]:=Abs[{(k2
κh1)/k1 ,κh2}.{h1[n,k1, k2,λ1,λ2,μ1,μ2,ν1,ν2,β,p,f,κh1,κa1,κh2,κa2,0.05],h2[n,k1,
k2,λ1,λ2,μ1,μ2,ν1,ν2,β,p,f,κh1,κa1,κh2,κa2,0.05]}]
        meansquare[n_,k1_,

k2_,λ1_,λ2_,μ1_,μ2_,ν1_,ν2_,β_,p_,f_,κh1_,κa1_,κh2_,κa2_]:=(forcefun[n,k1,

k2,λ1,λ2,μ1,μ2,ν1,ν2,β,p,f,κh1,κa1,κh2,κa2]*1546.651786*28)^2/2
```

References

Bansal, *Free waves in periodically disordered systems: Natural and bounding frequencies of unsymmetric systems and normal mode localization.* Journal of Sound and Vibration, Vol. 207 (3), 365-382, 1997.

Donald B. Bliss, *Noise Reduction Barriers that Inherently Resist Sound and Vibration Transmission.* Honda Initiation Grant 2008 Full-Proposal Submission, 2008.

William G. Bousman, *Estimation of Blade Airloads from Rotor Blade Bending Momnets,* NASA Technical Memorandum 100020, 1987.

Carcaterra and Bernardini, C., *Trapping of vibration energy into a set of resonators: Theory and application to aerospace structures.* Mechanical Systems and Signal Processing, Vol. 26, 1-14, 2012.

Cavallo, *Active Control of Flexible Structures: From Modeling to Implementation.* Springer, London, 2010.

Matthew W. Floros, *elastically tailored composite rotor blades for stall Alleviation and vibration reduction.* The Pennsylvania State University, 2000

Fuller, *Active Control of Vibration.* Academic Press, San Diego, 1996.

Bryan Glaz, *Active/Passive Optimization of Helicopter Rotor Blades for Improved Vibration, Noise, and Performance Characteristics.* University of Michigan, 2008.

Lee, *Noise reduction of passive and active hybrid panels.* Smart Materials & Structures, Vol. 11 (6), 940-946, 2002.

Legault, J, Atalla, N, *Numerical and experimental investigation of the effect of structural links on the sound transmission of a lightweight double panel structure*. Journal of Sound and Vibration, Vol. 324, 712-732, 2009.

Ohayon, R and Soize, C., *Structural Acoustics and Vibration: Mechanical Models, Variational Formulations and Discretization*. Academic Press, San Diego, 1998.

Photiadis, DM, and Houston, BH, *Anderson localization of vibration on a framed cylindrical shell.* Journal of the Acoustical Society of America, Vol. 106 (3), 1377-1391, 1999.

J. P. Rabbott. Jr., *A presentation of measured and calculated full-scale rotor blade aerodynamic and structural loads.* U. S. army aviation materiel laboratories, Fort Eustis, Virginia, 1966.

Silva, *Study of pass and stop bands of some periodic composites*. Acustica, Vol. 75 (1), 62-68, 1991.

Thompson, *A continuous damped vibration absorber to reduce broad-band wave propagation in beams*. Journal of Sound and Vibration, Vol. 311, 824-842, 2008.

Zielinski, *Numerical investigation of active porous composites with enhanced acoustic absorption.* Journal of Sound and Vibration, Vol. 330, 5292-5308, 2011.